Simultaneous and efficient utilization of photoelectrons and holes: A case of single-atom Pd-anchored CdS twins

Yuan Tang[1], Zhong-Fei Xu[3], Yan Sun[1], Chunyang Wang[2], Yuchen Guo[1], Weichang Hao[4]*, Xin Tan[1], Jinhua Ye[5], Tao Yu[2]*

[1]*School of Environmental Science and Engineering, Tianjin University, Tianjin 300350, China*

[2]*School of Chemical Engineering and Technology, Tianjin University, Tianjin 300350, China*

[3]*MOE Key Laboratory of Resources and Environmental Systems Optimization, College of Environmental Science and Engineering, North China Electric Power University, Beijing 102206, China*

[4]*School of Physics, Beihang University, Beijing 100191, China*

[5]*Research Center for Solar Driven Carbon Neutrality, Hebei University, Baoding 071002, China*

**Corresponding Author.*

E-mail address: yutao@tju.edu.cn (T. Yu)

whao@buaa.edu.cn (W. C. Hao)

Contents

Methods

Experimental materials

Lactic acid and Pyruvic acid were purchased from Tianjin Yuanli Chemical Co., Ltd. The reagents used in the experiment included Deionized water, Ethanol (95%) (C_2H_6O) and Triethanolamines ($C_6H_{15}NO_3$), Thioacetamide (TAA, CH_3CSNH_2), Cadmium acetate (Cd $(CH_3COOH)_2 \cdot 2H_2O$), Sodium sulphide ($Na_2S \cdot 9H_2O$), Sodium sulfite (Na_2SO_3), Palladium nitrate ($Pd(NO_3)_2$) and 2,2,6,6-Tetramethylpiperidine-N-oxide (TEMPO), were purchased from Shanghai Aladdin Biochemical Technology Co., Ltd. All the above experimental materials are analytically pure without further purification.

Synthesis of the photocatalysts

Typically, the amount of $Cd(CH_3COOH)_2 \cdot 2H_2O$ was dissolved in 30 mL of deionized water followed by the addition of CH_3CSNH_2 to form a homogeneous mixture, which was transferred to a Teflon-lined stainless steel autoclave and heated for 24 h at 180 °C. The precipitate was separated after cooling and washed several times with distilled water and anhydrous ethanol. The solvent was removed in a vacuum oven

at room temperature and the CdS_x was collected.

CdS_x sample powder was immersed in a certain amount of lactic acid dispersion of M ions for 2 h in situ photoreduction (full light irradiation) to form M-CdS_x-Twins, which were obtained as CdS_x-Twins containing a variety of metals, including Ag, Cu and Pt. For pure CdS_x-Twins, CdS_x sample powder was immersed into a certain amount of lactic acid dispersion for in situ photoreduction (1-3h), washed several times with distilled water and anhydrous ethanol, and the solvents were removed by vacuum oven at room temperature to form CdS_x-Twins.

20 mg of CdS_x sample powder was immersed in a certain amount of $Pd(NO_3)_2$ (>98.5%; Aladdin Biochemical Technology Co., Ltd.) lactic acid solution, and the catalyst was dispersed by strong sonication and continuous stirring to simultaneously adsorb Pd species on the CdS_x surface. The Pd species was loaded onto the prepared CdS_x photocatalyst by in-situ photoreduction procedure (300 W xenon lamp, full light irradiation). Through the controlled solution concentration of $Pd(NO_3)_2 \cdot H_2O$, different mass fractions of Pd-CdS_x-Twin were obtained, labeled as $_{0.07}$Pd-CdS_x-Twin, $_{0.3}$Pd-CdS_x-Twin, and $_{1}$Pd-CdS_x-Twin, respectively. After 1-3 h of photoirradiation under vacuum, the product was washed several times with water and ethanol and dried overnight in a vacuum oven at 60℃ to obtain Pd-CdS_x-Twin.

To clarify the actual content of Pd, ICP-MS of the prepared Pd-CdS_x-Twins was performed. The results revealed that the theoretical weight percentage content of Pd $(NO_3)_2 \cdot H_2O$ was 0.07%, 0.3% and 1% corresponding to actual Pt loadings of 0.11%, 0.34% and 1.08%, respectively (Table S1).

Table S1 The actual elemental content of Cd, S and Pd in Pd-CdS_x-Twins.

Samples	Elemental content of Cd ($_{wt}$%)	Elemental content of S ($_{wt}$%)	The molar ratio of S:Cd	Elemental content of Pd ($_{wt}$%)
$_{0.07}$Pd-CdS_x-Twins	74.61	25.27	1.19	0.11%
$_{0.3}$Pd-CdS_x-Twins	74.42	25.21	1.19	0.34%
$_{1}$Pd-CdS_x-Twins	73.89	25.03	1.19	1.08%

Photoelectrochemical measurements

The photochemical tests were performed on a CHI660C electrochemical workstation (Chenhua Instruments, China) using a standard three-electrode system, where the electrolyte was 50 mL of Na_2SO_4 electrolyte (0.1 M) and 0.25vol.LA. Ag/AgCl and Pt sheets (1 cm × 1 cm) were used as the reference and counter electrodes, respectively, and indium tin oxide (ITO) transparent conductive glass coated with samples as the working electrode. For the working electrode, 20 mg of catalyst was dispersed in 10 mL of ethanol by adding 20 μL of 5% Nafion solution. Then it was dispersed on the conductive surface of the ITO glass and dried overnight at 60 ℃. Mott-Schottky curves were collected at a frequency of 900 Hz. The electrochemical impedance spectra were performed at an open circuit voltage of 0.3 V and a frequency range of 0.01 to 1×10^5 Hz. The transient photocurrent response curve was measured under visible light ($\lambda \geqslant 420$ nm) irradiation, and the run time was 440 s, the applied potential was −0.2 V. The EIS pattern under light conditions in 0.25% vol. lactic acid,

irradiated externally with a 300 W xenon lamp. The distance between the working electrode and the center of the lamp was 5.0 cm. the actual exposed area of the electrode during the photoelectrochemical tests was 4.5 cm^2. the EIS was tested at a magnitude of 5 mV and a frequency range of 10^{-2}-10^5 Hz.

Materials characterization

The microscopic morphology and lattice structure of $_{0.3}$Pd-CdS_x-Twin and CdS_x were obtained by FEI Tecnai G2 F200 transmission electron microscopy (TEM, The Netherlands) with its accompanying high-angle annular dark field (HAADF) and Energy Dispersive Spectrometer (EDS) images. The physical phase structures of $_{0.07}$Pd-CdS_x-Twin, $_{0.3}$Pd-CdS_x-Twin, and $_{1}$Pd-CdS_x-Twin and CdS_x were analyzed by Raman spectroscopy (excitation wavelength 532 nm, XPLORA plus, France) and X-ray diffractometry (XRD, Bruker D8-Focus, Germany). The optical properties of the prepared materials were evaluated by obtaining UV-vis diffuse reflectance spectra (UV-vis DRS) using a UV-3600 UV-vis spectrophotometer (excitation wavelength of 365 nm, Japan). The Thermo Scientific X-ray photoelectron spectroscopy (XPS, Al Kα source, USA) was characterized for analyzing the chemical state of the prepared samples. The photogenerated electron-hole recombination rate of the materials was performed by a Fluorolog-3 fluorescence spectrophotometer Photoluminescence (PL) spectral measurements (excitation wavelength of 330 nm, Hitachi, Japan). Time-resolved photoluminescence (TRPL) spectra were recorded on a FLS1000 fluorescence lifetime spectrophotometer (UK), TRPL was performed at an excitation wavelength of

390 nm and monitoring wavelength of 475 nm. Surface potential measurements under dark and surface photovoltage under illumination were measured by a Kelvin probe force microscope (KPFM) configured with a 300 W Xe lamp source. Prior to testing, the probe was calibrated with an iron sheet and the test sample was uniformly dispersed on the conductive iron sheet. The electron spin resonance spectra (ESR) were obtained electronically using a JES-FA200 (Japan) spectrometer for detecting the presence of S vacancies and surface unsaturated S. In situ XPS was measured using an ESCALAB250Xi X-ray photoelectron spectrometer (Thermo Scientific) with Al Kα as the excitation source and equipped with a 300 W Xe lamp (CEL-HXF300, CEAULICHT) with a 400 nm filter. During the test, the light source was placed about 30 cm away from the sample. Pd *K*-edge analysis was performed with Si(311) crystal monochromators at the BL14W1 beamlines at the Shanghai Synchrotron Radiation Facility (SSRF) (Shanghai, China). Before the analysis at the beamline, samples were pressed into thin sheets with 1 cm in diameter and sealed using Kapton tape film. The XAFS spectra were recorded at room temperature using a 4-channel Silicon Drift Detector (SDD) Bruker 5040. Pd *K*-edge extended X-ray absorption fine structure (EXAFS) spectra were recorded in fluorescent mode. Negligible changes in the line-shape and peak position of Pd *K*-edge XANES spectra were observed between two scans taken for a specific sample. The XAFS spectra of these standard samples (PdO, Pd-CdS_x-Twins, Pd foil) were recorded in fluorescent mode. The spectra were processed and analyzed by the software codes Athena and Artemis.

The fs-TA measurements were performed on a Helios pump-probe system

(Ultrafast Systems LLC) combined with an amplified femtosecond laser system (Coherent). Optical parametric amplifier (TOPAS-800-fs) provided a 400 nm pump pulse (~ 0.35 uj/cm^2), which was excited by a Ti: sapphire regenerative amplifier (Legend Elite-1K-HE; 800 nm), 35 fs, 7 mJ/pulse, 1 kHz) and seeded with a mode-locked Ti: sapphire laser system (Micra 5) and an Nd: YLF laser (EvolutIon 30) pumped. Focusing the 800 nm beams (split from the regenerative amplifier with a tiny portion, ~400 nJ/pulse) onto a sapphire plate produced the white-light continuum (WLC) probe pulses (450-770 nm). The pulse-to-pulse fluctuation of the WLC is corrected by a reference beam split from WLC. A motorized optical delay line was used to change the time delays (0-8 ns) between the pump and probe pulses. The instrument response function (IRF) was determined to be ~100 fs by a routine cross-correlation procedure. The instrument response function (IRF) was determined to be ~100 fs by a routine cross-correlation procedure. A mechanical chopper operated at a frequency of 500 Hz used to modulate the pump pulses such that the fs-TA spectra with and without the pump pulses can be recorded alternately.

Photocatalytic H_2 evolution and pyruvate synthesis

The photocatalytic performance evaluation was carried out in a 350 mL closed reaction tank. Photocatalytic hydrogen release and pyruvate production performance were tested in the full spectral range of visible light ($\lambda \geq 420$) using a 300 W xenon lamp as a light source. 50 mg of photocatalyst was dispersed in aqueous lactic acid solution (10 vol%, 1 vol%, 0.4 vol%, 0.25 vol%, 0.1 vol%). The reaction gas lines were

evacuated to remove excess gas from the system before turning on the lights. The temperature of the reaction system is continuously controlled by a cooling circulating water system at 10 °C. The product was exported from the reaction tank at each hour of the reaction. The concentration of H_2 was analyzed by an on-line GC-14C gas chromatograph (Shimadzu, Japan) with a thermal conductivity detector (TCD). Pyruvic acid concentration was detected by an Agilent LC1260 Infinity HPLC equipped with a UV-visible detector (1260 DAD, Aglient, USA). The analytical conditions were as follows: the mobile phase was 10 mM potassium dihydrogen phosphate solution at a flow rate of 1.0 mL min^{-1}.

The conversion of LA and selectivity of PA were calculated by the following:

$$Conversion(\%) = \frac{C_0 - C_r}{C_0} \times 100\% \qquad (S1)$$

$$Selectivity(\%) = \frac{C_p}{C_0 - C_r} \times 100\% \qquad (S2)$$

$$Yeid\ (\%) = Conversion \times Selectivity \qquad (S3)$$

C_0 denotes the initial concentration of reactants, and the concentration of reactants and products after a certain period of the photocatalytic reaction is denoted by C_r and C_p.

Apparent quantum efficiency (AQE) measurements were performed using a 300 W xenon lamp as the light source. Monochromatic light was obtained by filtering through band-pass filters of different wavelengths. AQE was calculated according to the following equation:

$$AQE = \frac{number\ of\ photons\ utilized\ in\ H_2\ evolution}{total\ number\ of\ photons} = \frac{2R_{H_2}N_A}{n} \qquad (S4)$$

($R_{H_2} = H_2\ production\ rate, N_A = Avogadro\ constant$)

The number of moles of photons irradiated to the system in the corresponding time was measured through the following method: The spectrum and optical density were collected by an AvaSolar-1 fiber optic spectrometer from Avantes, USA. As shown in Scheme S1, the distance between the probe and the xenon lamp before the test was adjusted to the distance between the xenon lamp and the liquid surface during the photocatalytic reaction. After fixing the distance between the xenon lamp and the probe, the xenon lamp was equipped with the corresponding filter or monochromator, and nine points were selected and measured separately and averaged. The transmittance area of the nine points was 17.2cm^2. For the performance of the sunlight simulation with different light intensities, the light intensity was adjusted by adjusting the xenon lamp current (16A, 17A, 18A, 19A). In this work, bandpass filters of 420, 470, 500, 560 nm, 650 and 750 nm (Newbit, China) were used to obtain monochromatic excitation light (Table S2a).

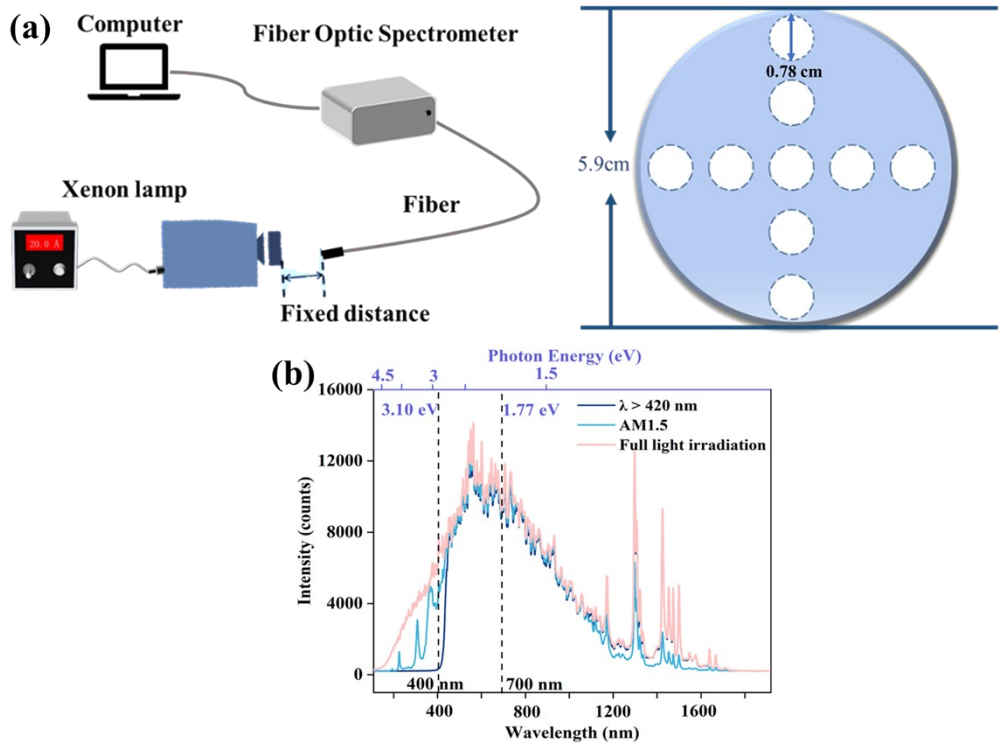

Scheme S1. (a) Illustration of light intensity measurement equipment. (b) The spectrum of irradiation at full light irradiation, with AM1.5 filter and visible light filter.

Table S2a. The data of the irradiation intensity testing with different wavelength.

Wavelength（nm）	400	420	450	470	500	550
Irradiation intensity (μmol/s/m^2)	240.5	245.4	272.2	304.7	314.6	419.8

Table S2b. Irradiation intensity with different Xenon lamp filters

Xenon lamp filters	full-light irradiation	AM 1.5	λ ≥ 420
Irradiation intensity (mW/cm^2)	1125	950	802

Experiments on the activation energy of photocatalytic hydrogen evolution at different temperatures: the reaction temperature was controlled by condensing water at 4, 8, 12 and 16 °C to measure the rate of photocatalytic hydrogen evolution at different temperatures. Here, the apparent activation energy (E_a) of photocatalytic hydrogen evolution of the prepared samples was calculated according to the Arrhenius equation as follows:

$$lnk = -\frac{E_a}{RT} + lnA \qquad S5$$

where A was the frequency factor, T was the thermodynamic temperature of the reaction, E_a was the apparent activation energy, k was the reaction rate constant, and R was the molar gas constant."

Theoretical calculation details

DFT calculations are carried out by Vienna Ab initio Simulation Package(VASP). The exchange-correlation interaction is described by generalized gradient approximation (GGA) with the Perdew-Burke-Ernzerhof (PBE) function. The cutoff energy was set as 400 eV and gamma only point was used because the large supercell. All atoms are fully relaxed with the energy convergence tolerance of 10^{-4} eV per atom, and the final force on each atom is converged to 0.02 eV/Å.

The free energies of reaction intermediates are calculated at 298 K, according to

the equation as following.

$$G = E + EZPE - TS \qquad (S6)$$

where E is the total energy of the system adsorbed with intermediates. E_{ZPE} and S is the zero-point energy and entropy of intermediates, respectively. The values of E_{ZPE} and S can be obtained by vibration frequency calculation.

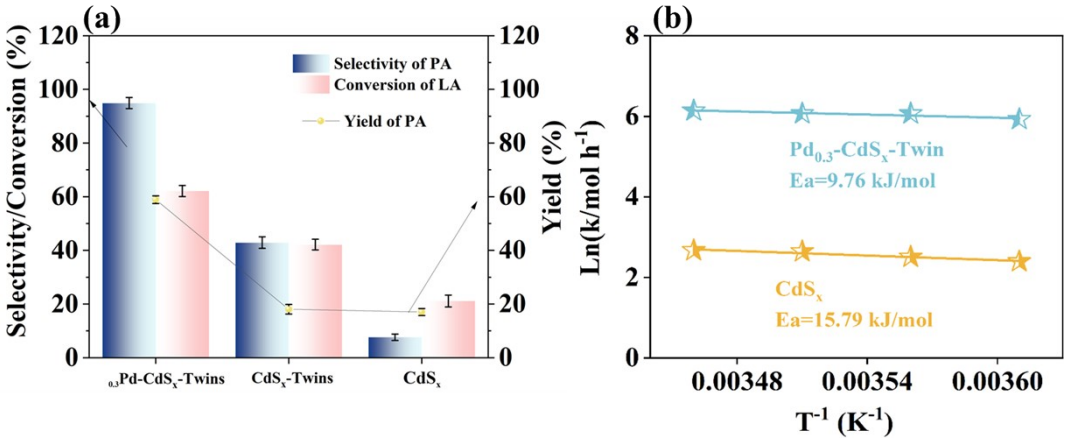

Figure S1. (a) The yield, conversion and selectivity data for Pd-CdS_x-Twin, CdS_x-Twin and CdS_x with error bars. (b)Apparent activation energy of $Pd_{0.3}$-CdS_x-Twins and CdS_x.

Table S3. Activation energies of reported dehydrogenation reactions

Catalyst	Dehydrogenation reactions	Activation energies	Ref.
Pd-TiO_2	Functionalization of benzene with ether upon	35.4 KJ/mol	[1]
DHN/TiO_2-Cu	Semi hydrogenation of alkynes to alkenes	27 KJ/mol	[2]
Pt/TiO_2	Cross-coupling between THF and cyclohexane	37 KJ/mol	[3]
Pd-CdS_x-Twins	**Conversion of lactic acid to pyruvic acid**	**9.76 KJ/mol**	**This work**

Discussion: By comparing the activation energies of reported dehydrogenation reactions, Pd-CdS_x-Twins have lower reaction activation energies in the LA selective generation of pyruvate (Table S3).

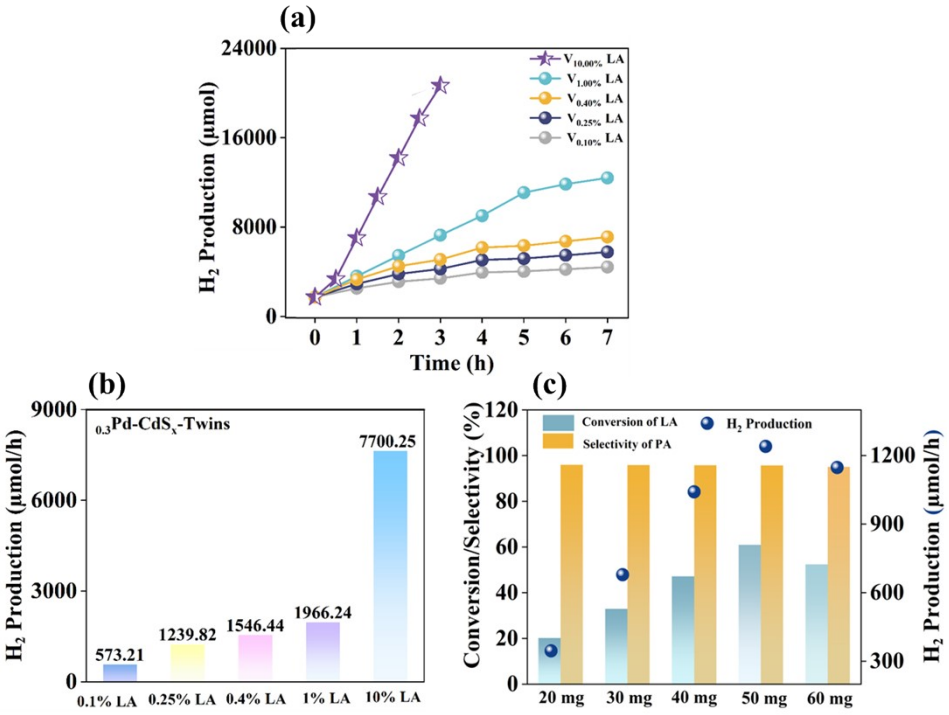

Figure S2. (a) Hydrogen extraction activity from different lactic acid concentrations of $Pd_{0.3}$-CdS_x-Twins. (b) Rates of hydrogen extraction from different lactic acid different volume fractions by $Pd_{0.3}$-CdS_x-Twins.Where 0.1% vol. 0.25% vol. 0.4% vol. 1% vol. and 10% vol. of lactic acid corresponds to 1.34 mmol, 3.35 mmol, 5.36 mmol 13.40 μmol and 134.0 mmol of lactic acid. (c) Photocatalytic H_2 evolution rates, conversion of LA and selectivity of PA for Pd-CdS_x-Twins with different masses.

Discussion：In this work, the variations in the concentration of lactic acid used are summarized as being in two different conditions with different functions. Firstly, during the preparation of the catalyst lactic acid acts as a hole trapping agent to provide opportunities for the formation of Pd single atoms and twins, where lactic acid is excessively involved in the reaction and there is no positive correlation between the

photocatalyst activity and the lactic acid concentration. Secondly, hydrogen evolution experiments of Pd-CdS_x-Twins were carried out at different lactic acid concentrations, where lactic acid was used as a reactant in the hydrogen extraction reaction, and there was a positive correlation between lactic acid concentration and photocatalyst activity, the photocatalytic activity decreasing with the depletion of the reactants. In addition, the mass of Pd-CdS_x-Twins samples for photocatalytic hydrogen evolution and pyruvic acid production is optimized, with 50 mg of the photocatalyst achieving optimal photocatalytic performance.

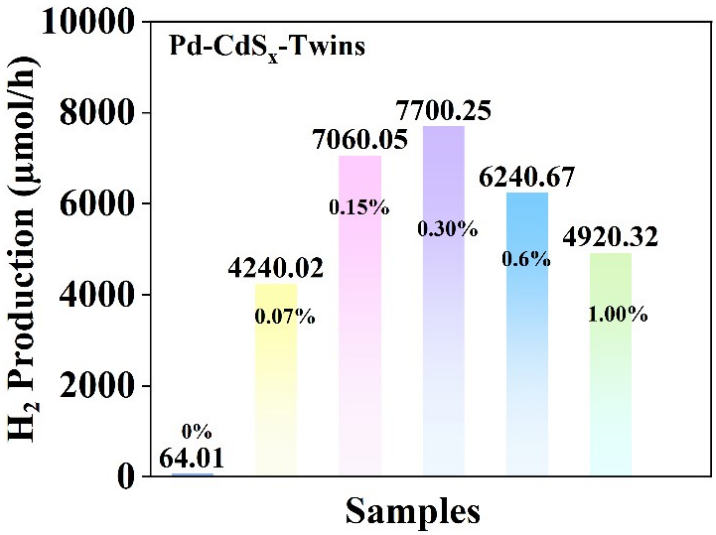

Figure S3. Rates of hydrogen extraction from 10% vol. lactic acid by Pd-CdS_x-Twins with different Pd loadings.

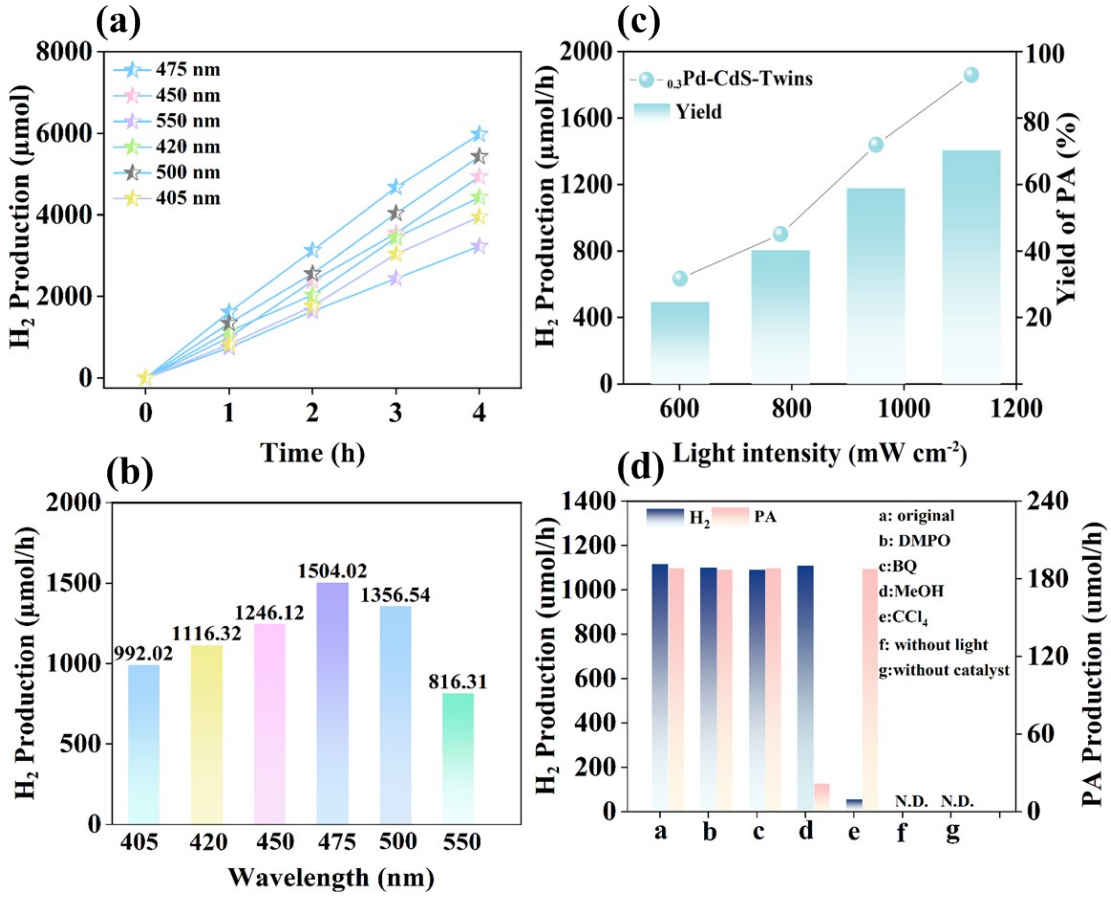

Figure S4. (a) Hydrogen extraction activity of $_{0.3}$Pd-CdS$_x$-Twins at different wavelengths. (b) Rates of hydrogen extraction for $_{0.3}$Pd-CdS$_x$-Twins at different wavelengths from 10% vol. lactic acid. (c) The photocatalytic performance of the $_{0.3}$Pd-CdS$_x$-Twins under simulated sunlight irradiation with different light intensities. (d) Controlled experiments on photocatalytic hydrogen evolution and PA production of Pd$_{0.3}$-CdS$_x$-Twins.

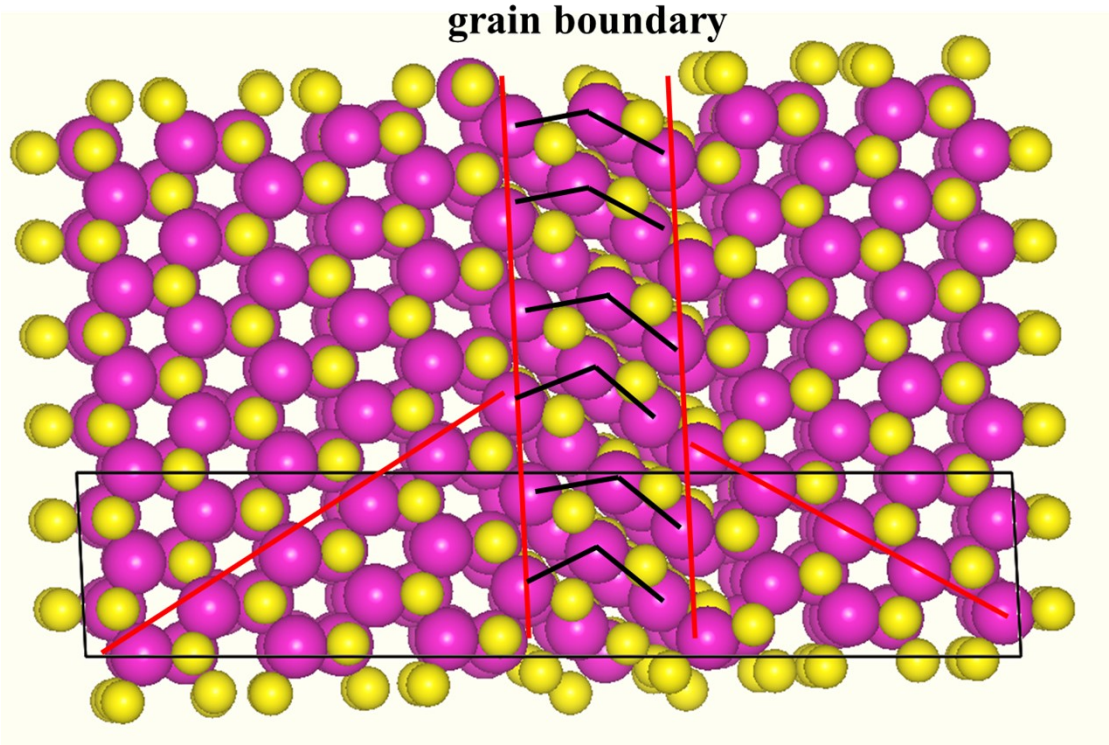

Figure S5. The (111)/[11-2] type coherent twin structure of CdS_x-Twin.

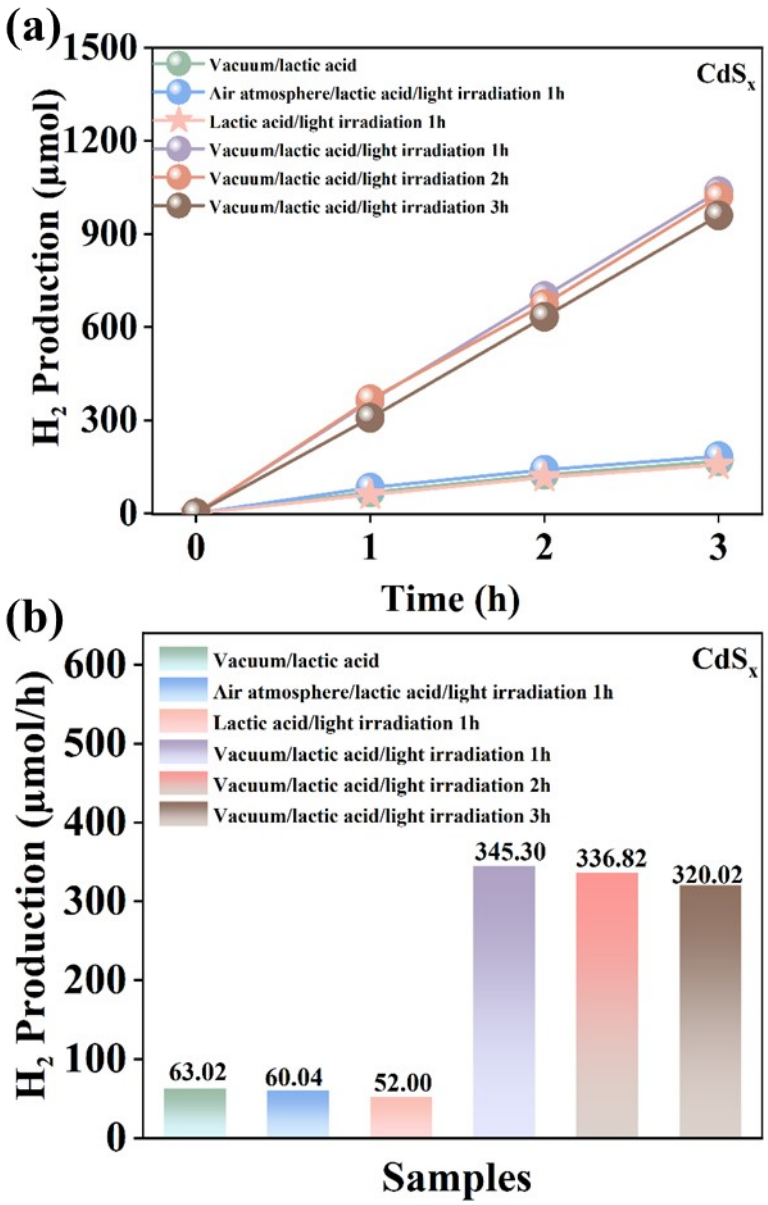

Figure S6. Activity of twinned CdS_x-Twins prepared by photo irradiation of CdS_x under different atmospheric conditions.

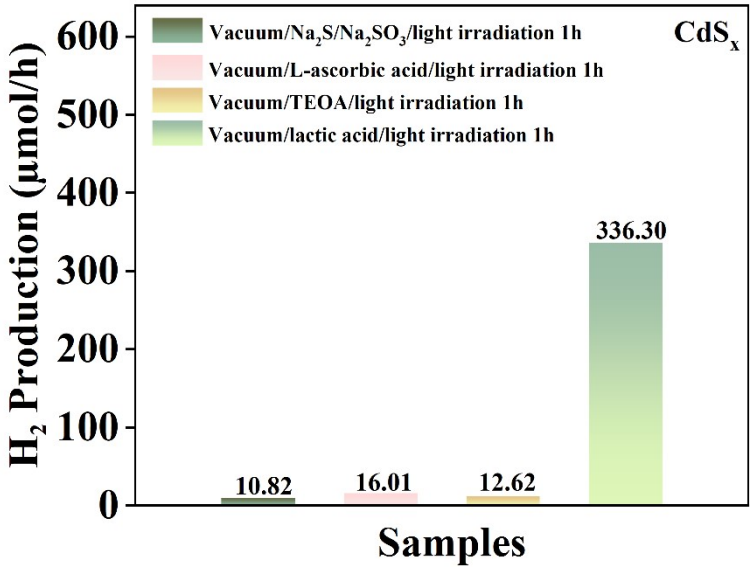

Figure S7. Activity of twinned CdS_x-Twins in different sacrificial agents for preparation of photo-irradiated CdS_x.

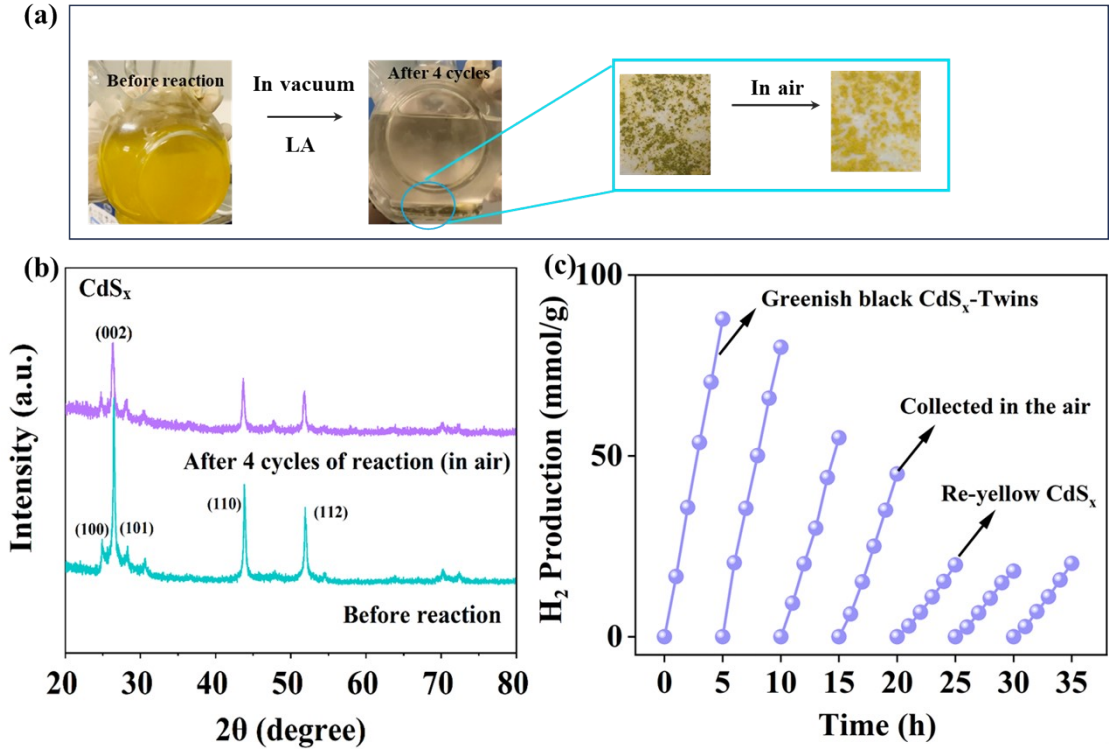

Figure S8. Cyclic Stability of CdS_x-Twins. (a) Color changes during the preparation of twinned CdS_x-Twins by photo irradiation of CdS_x. (b) XRD pattern of the original CdS_x before and after the reaction, the color of the greenish black in the reaction changed to yellow immediately after the CdS_x is placed in the air, and the XRD after the reaction is the re-yellowed CdS_x. (c) The hydrogen evolution performance for the first 20 hours is the cyclic performance of irradiated CdS_x-Twins, and as the cyclic performance decreases, the CdS_x-Twins are collected in air, and the hydrogen evolution performance for the last 15 hours is the cyclic performance of Re-yellow CdS_x.

Discussion: It is well known that the light intensity of a xenon lamp with a filter will be attenuated to a certain extent. The difference between the energy of full xenon lamp irradiation and filters is significant in terms of light intensity and spectrum. The

spectrum of irradiation at full light irradiation, with AM1.5 filter and visible light filter is shown in Figure Scheme S1b. There is a significant disparity in the UV region, where the full band of radiation contains short-wave UV light that is not present in sunlight and the photon energy of the UV light is the strongest in the entire region. The LA dehydrogenation process allows the CdS_x surface with unsaturated edge S to have sufficient conditions for adsorption of more active hydrogen. It is reasonable to speculate that exposure to the energy of the UV-irradiated region leads to the formation of tensile strains and lattice dislocations more readily in catalysts after adsorption with active hydrogen.

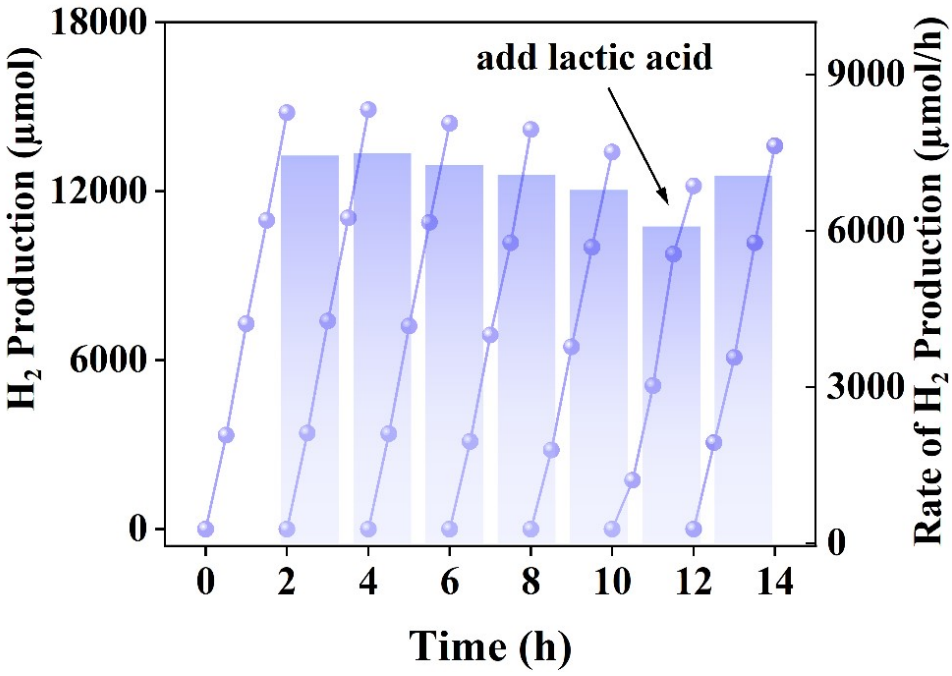

Figure S9. Cyclic stability of $Pd_{0.3}$-CdS_x-Twins for hydrogen extraction in 10 vol. LA.

Discussion: Since the concentration of the reactant is not updated, after five consecutive cycles the activity decreases with the depletion of lactic acid. However, the activity recovered after replenishment of lactic acid, which further demonstrated the cyclic stability of the catalyst.

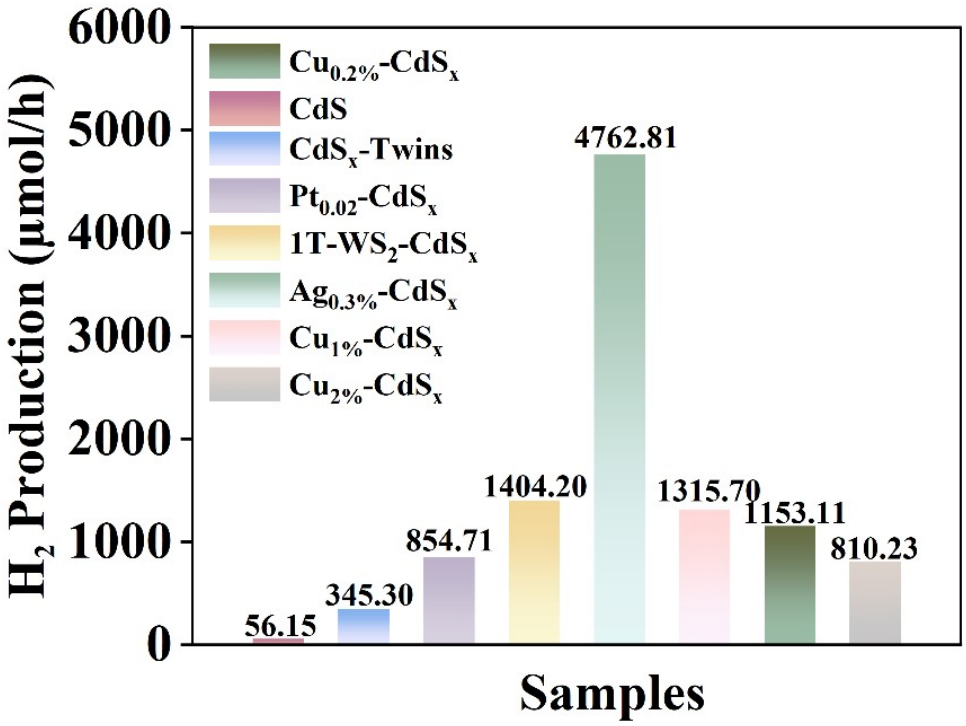

Figure S10. The performance of CdS_x-Twins loaded with other co-catalysts in the extraction of hydrogen from lactic acid.

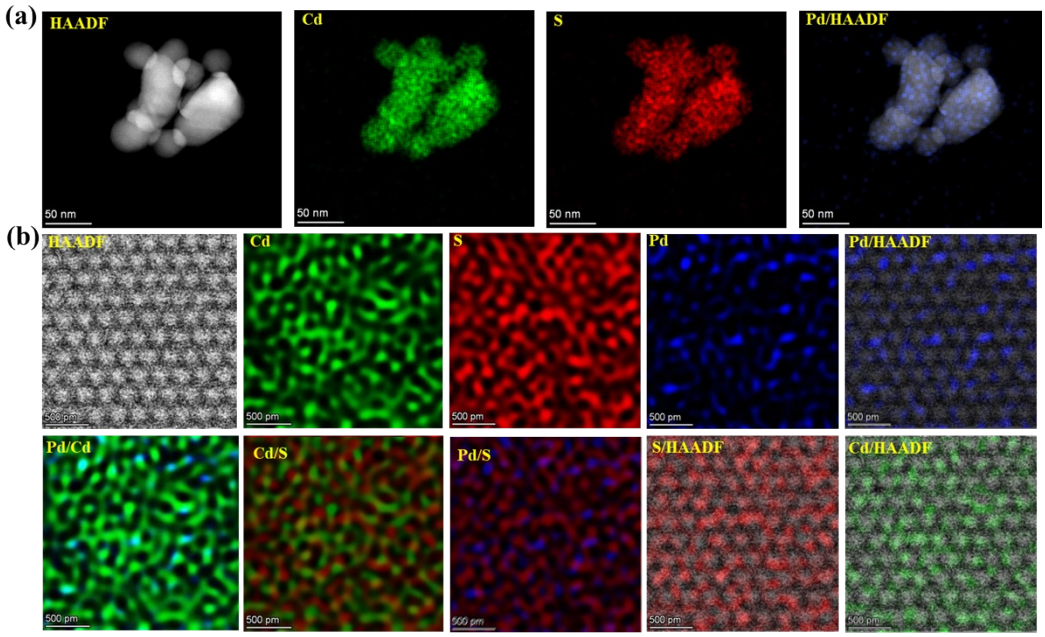

Figure S11. (a) The high-resolution TEM image (HRTEM) and Element mapping image of $Pd_{0.3}$-CdS_x-Twin at 50nm. (b) The Element mapping image of Spherical aberration corrected Transmission Electron Microscope (ACTEM) for Pd-CdS_x-Twin at 500 pm.

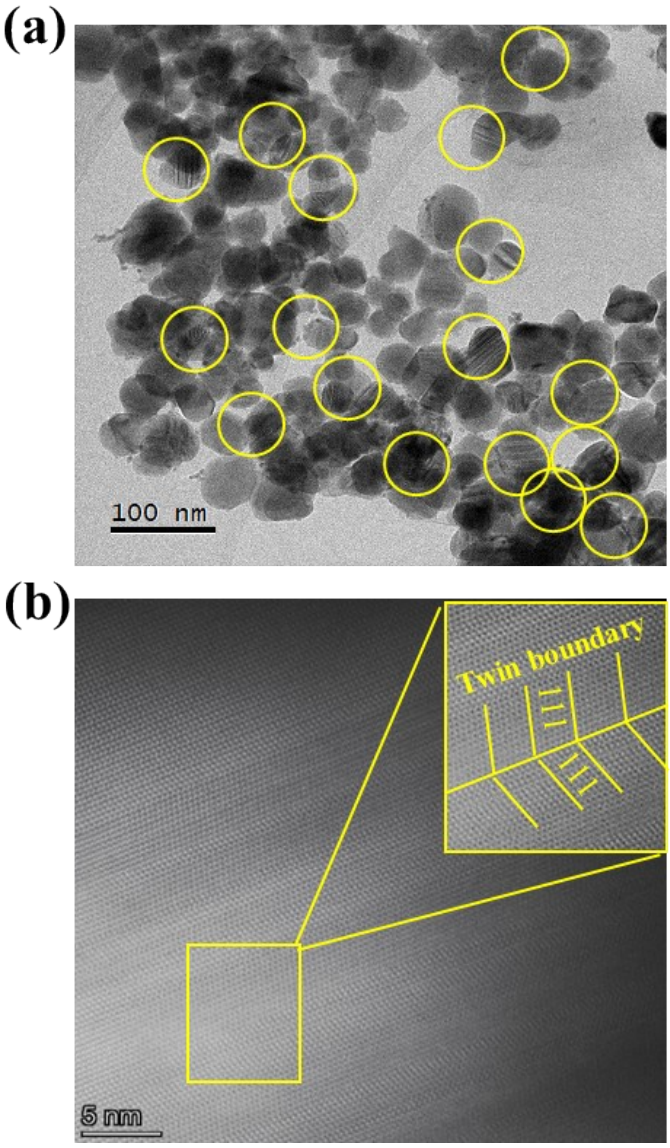

Figure S12. (a) TEM images of $Pd_{0.3}$-CdS_x-Twins and (b) HRTEM images at 5 nm demonstrate the presence of CdS_x-Twins.

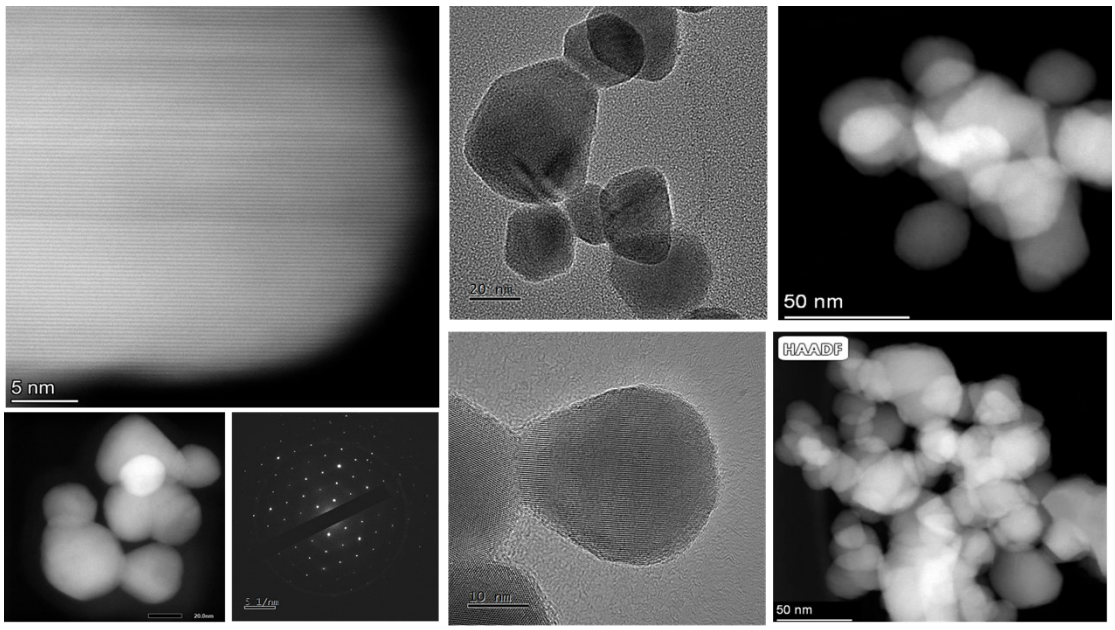

Figure S13. HRTEM and dark field images of pristine CdS_x without twins.

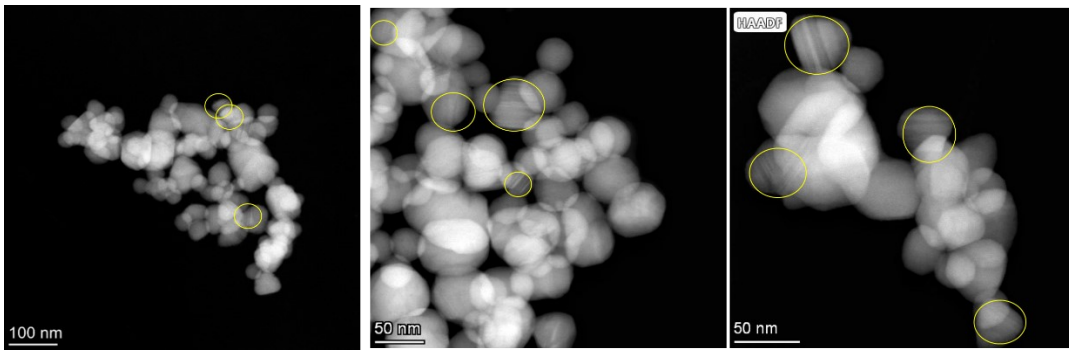

Figure S14. Multiple view dark-field TEM image of $Pd_{0.3}$-CdS_x-Twins, the yellow circled portion is identified as a twin.

Discussion: The dark-field image of the twin under the transmission electron microscope has certain characteristics of the contrast, which consists of parallel bands with black and white contrast and unequal widths. The same contrast bands are in the same orientation, while the other contrast band is in a symmetrical orientation. The base grain conforms to the Bragg equation, resulting in a bright contrast of the base in the dark field image. The twin crystal displays the darker contrast and thus exhibits two parallel sets of light and dark bands at the interface. In addition, the twins of Pd-CdS_x-Twins at high resolution are both found in such parallel bands with black and white contrast.

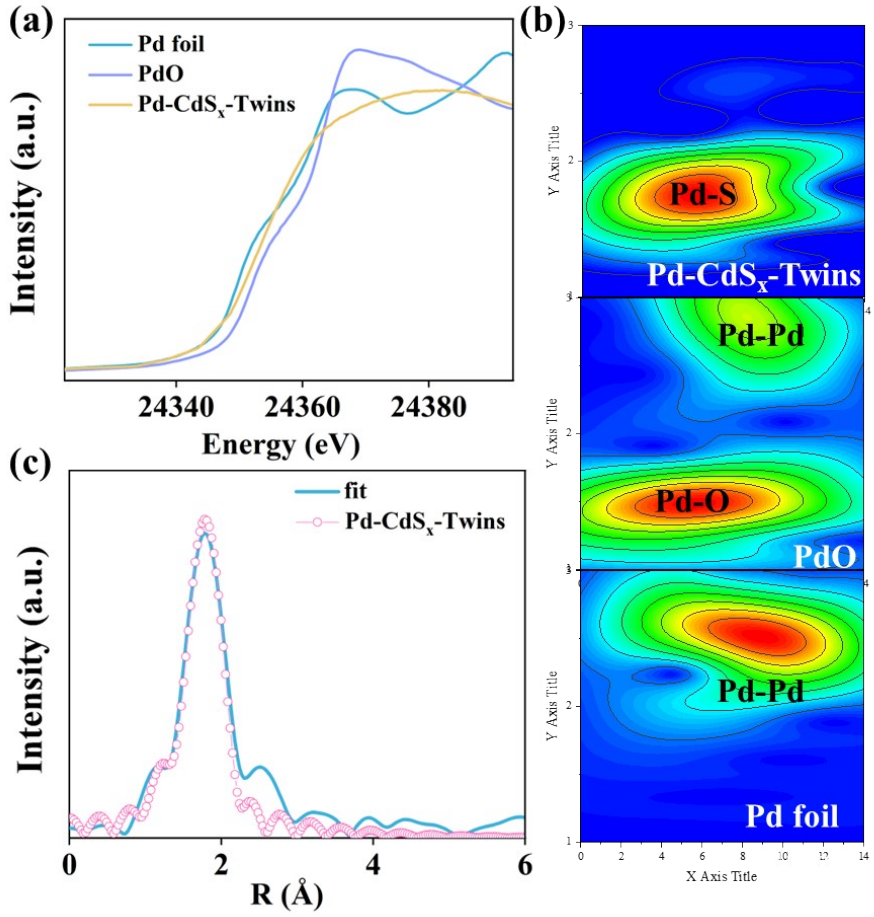

Figure S15. (a) X-ray absorption near-edge structure spectroscopy (XANES) of Pd foil, PdO and Pd-CdS_x-Twin. (b) Pd K-edge wavelet transform EXAFS of Pd foil, PdO and Pd-CdS_x-Twin. (c) The fitting results of the EXAFS data for Pd foil, PdO and Pd-CdS_x-Twin.

Table S4. Structural parameters extracted from EXAFS fitting.

Sample	Edge	Path	CN	R(Å)	σ^2(10^{-3} Å)	ΔE_0(eV)	R-factor
Pd-CdS_x-Twins	Pd-K	Pd-S	3.65	2.50	6.72	-0.53	0.016

Notes: CN, coordination number; R, distance between absorber and backscatter atoms. σ^2, Debye-Waller factor; ΔE_0, the inner potential difference between the reference compound and the experimental sample. R-factor, the goodness of fit.

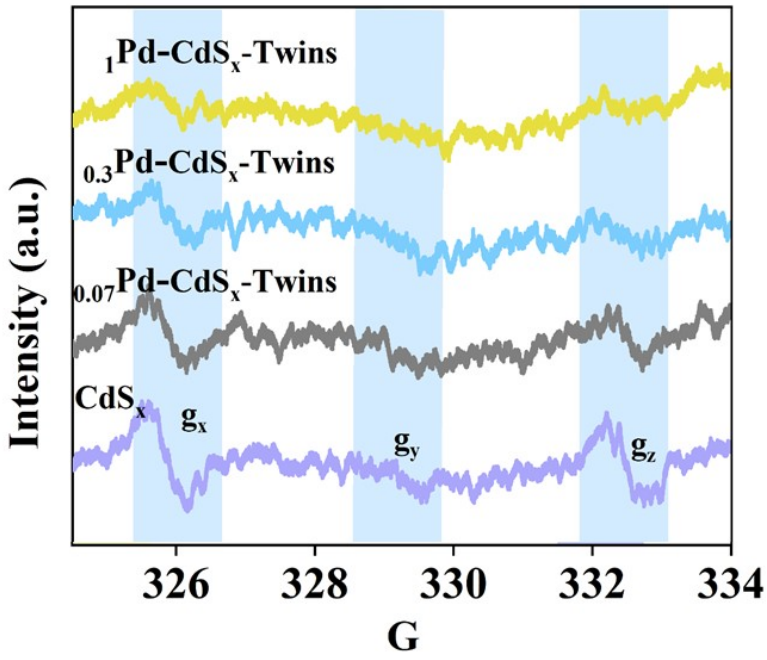

Figure S16. EPR spectra of CdS_x, Pd-CdS_x-Twins.

The signal peaks located at g_x=2.023, g_y=2.003 and g_z=1.983 in the EPR spectrum correspond to unsaturated S suspended on CdS_x, agreeing with the results of XPS [43].

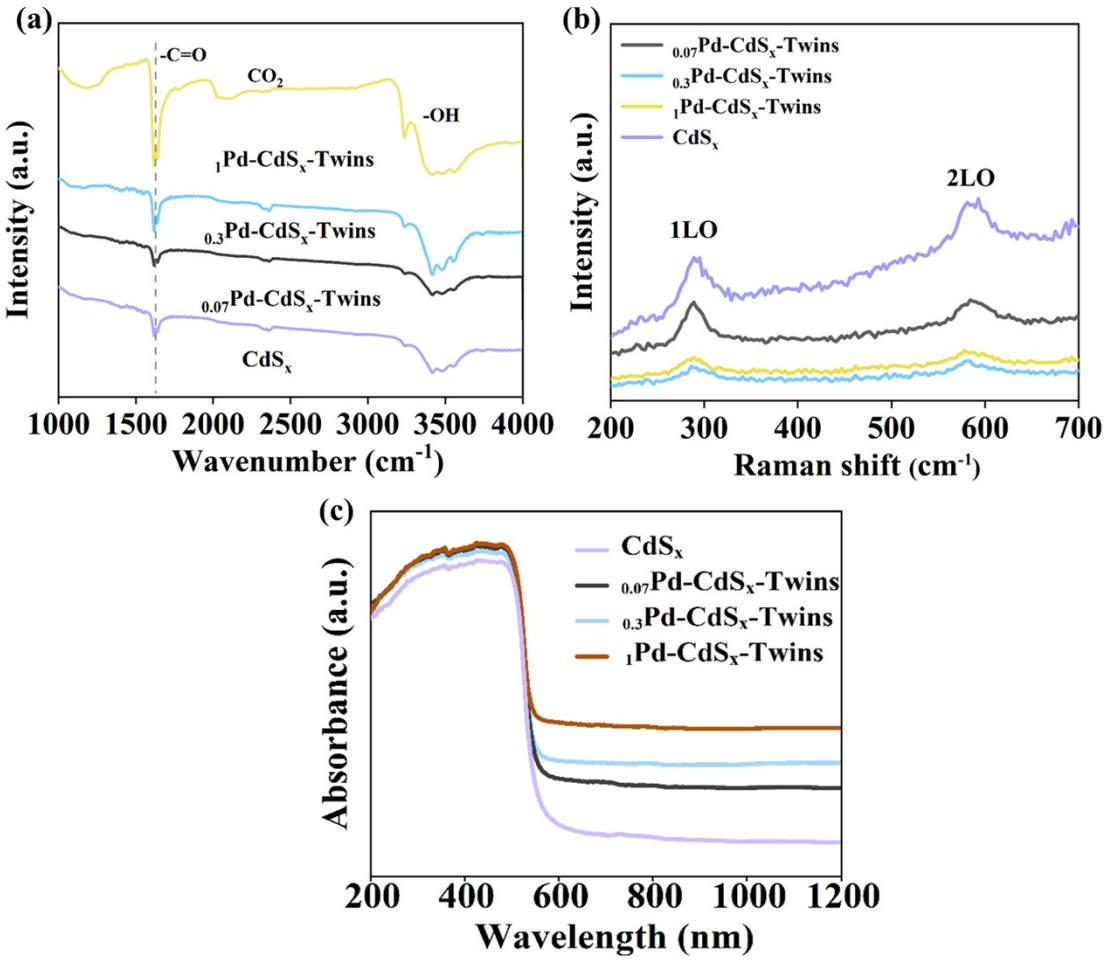

Figure S17. (a) FTIR spectrum. (b) Raman spectrum and (c) DRS spectrum of Pd-CdS_x-Twins and CdS_x.

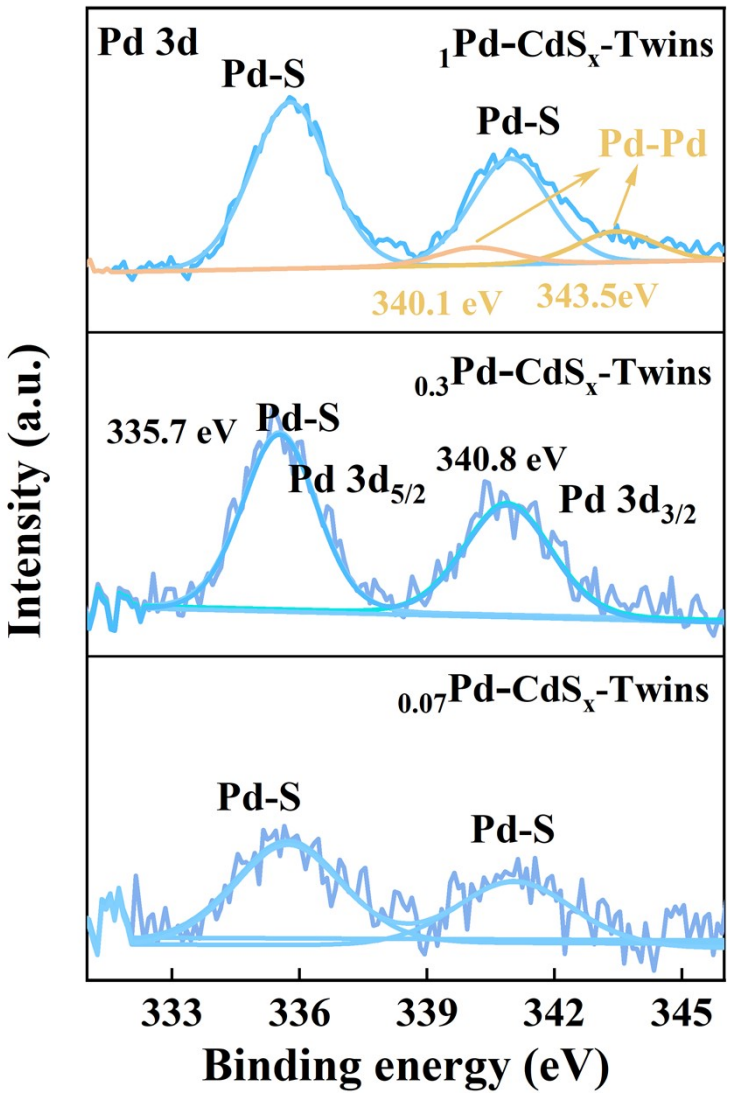

Figure S18. Pd 3d XPS patterns of Pd-CdS_x-Twins.

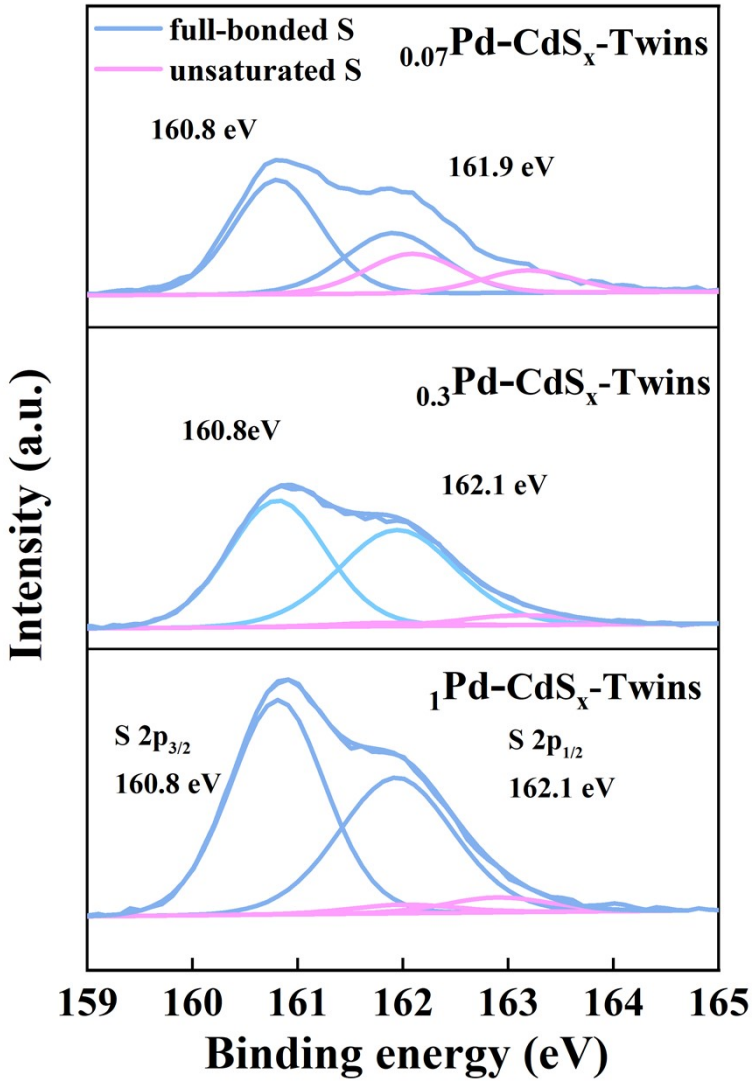

Figure S19. S 2p XPS patterns of Pd-CdS_x-Twins.

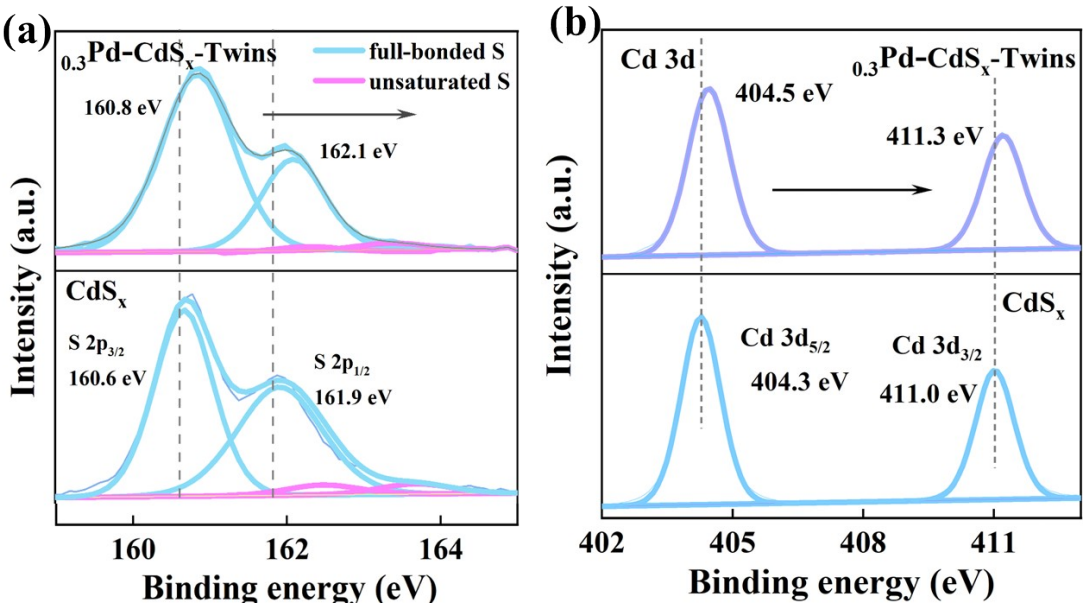

Figure S20. S 2p and Cd 3d XPS patterns of $_{0.3}$Pd-CdS$_x$-Twins and CdS$_x$.

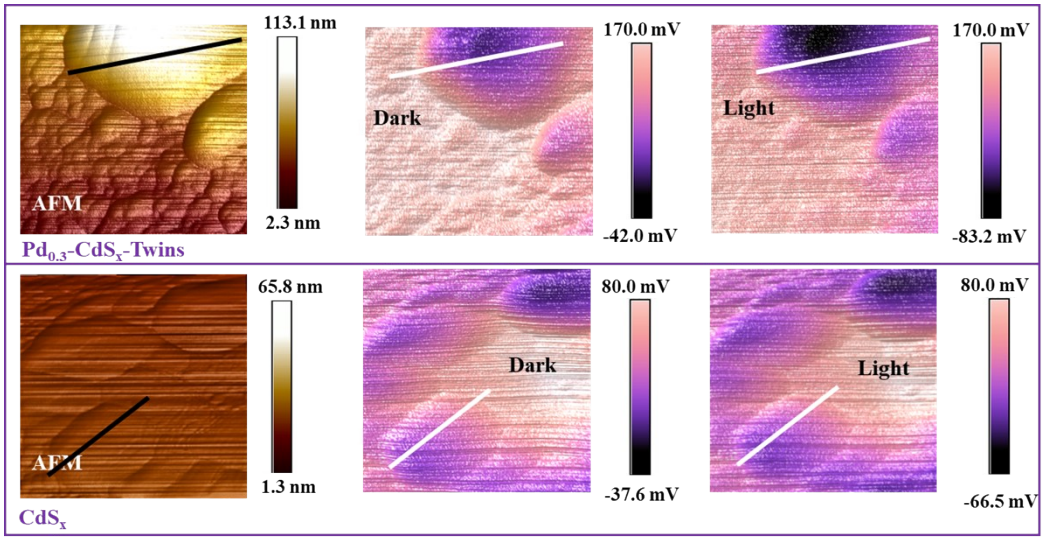

Figure S21. Correspondence of the potentials of CdS_x and $_{0.3}$Pd-CdS_x-Twins under dark and visible light irradiation with the thicknesses of CdS_x and $_{0.3}$Pd-CdS_x-Twins measured by atomic force microscopy (AFM).

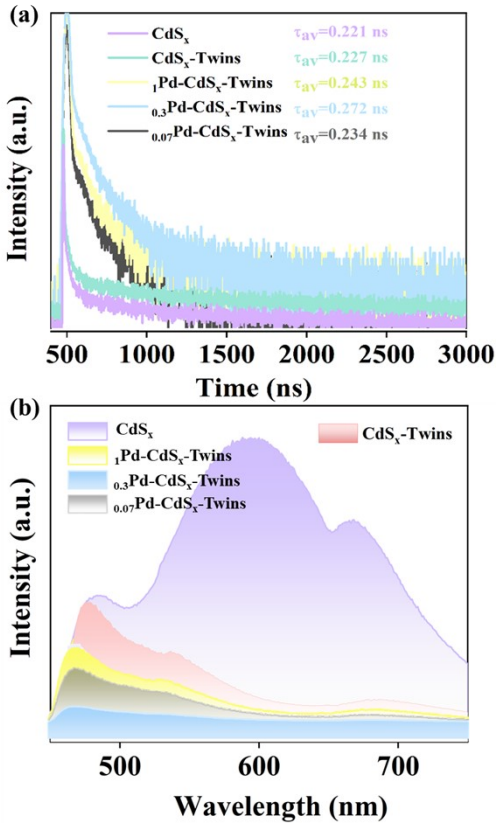

Figure S22. (a) Transient fluorescence emission (TRPL) spectra. (b) Photoluminescence (PL) spectrum of Pd-CdS_x-Twins and CdS_x.

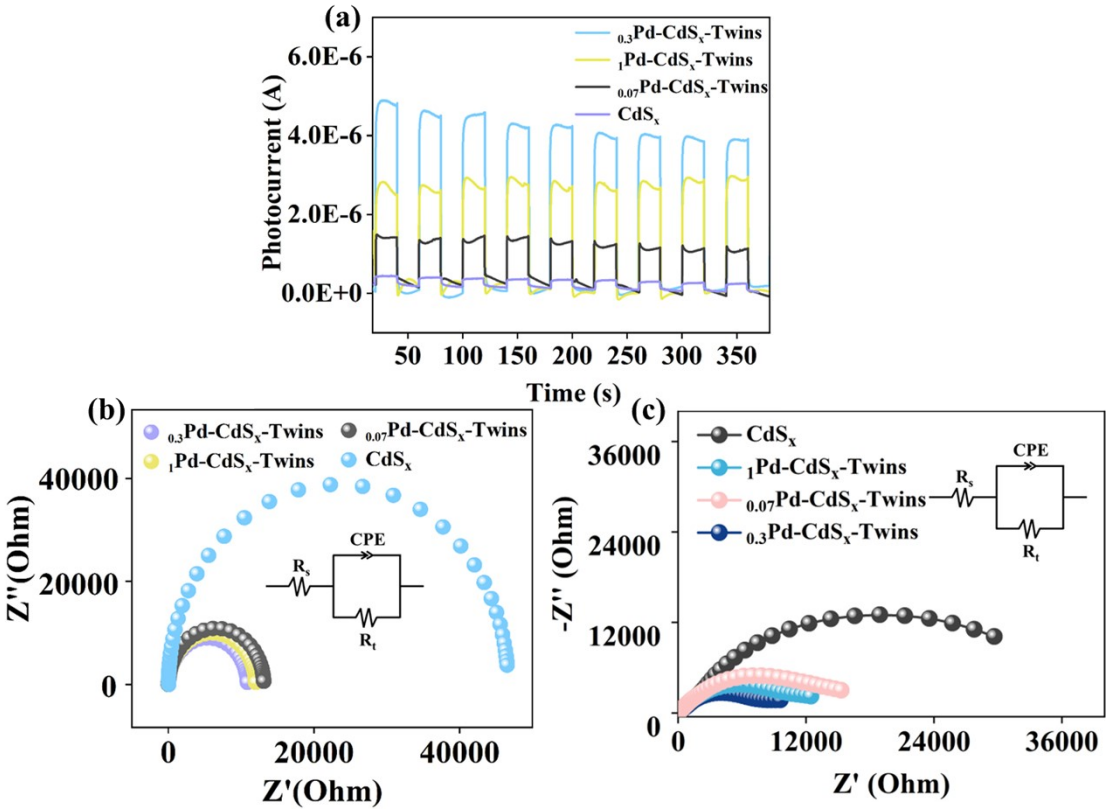

Figure S23. (a)Transient photocurrent response spectra and (b) EIS spectra of Pd-CdS_x-Twins and CdS_x (Electrolyte solutions: 0.1M Na_2SO_4). (c) EIS spectra of Pd-CdS_x-Twins and CdS_x (Electrolyte solutions: 0.25% vol. lactic acid).

Discussion: To verify the charge transfer rate at the electrode interface in actual photocatalysis, we supplemented the EIS pattern under light conditions in 0.25% vol. lactic acid, irradiated externally with a 300 W xenon lamp. The distance between the working electrode and the center of the lamp was 5.0 cm. the actual exposed area of the electrode during the photoelectrochemical tests was 4.5 cm^2. the EIS was tested at a magnitude of 5 mV and a frequency range of 10^{-2}-10^5 Hz.

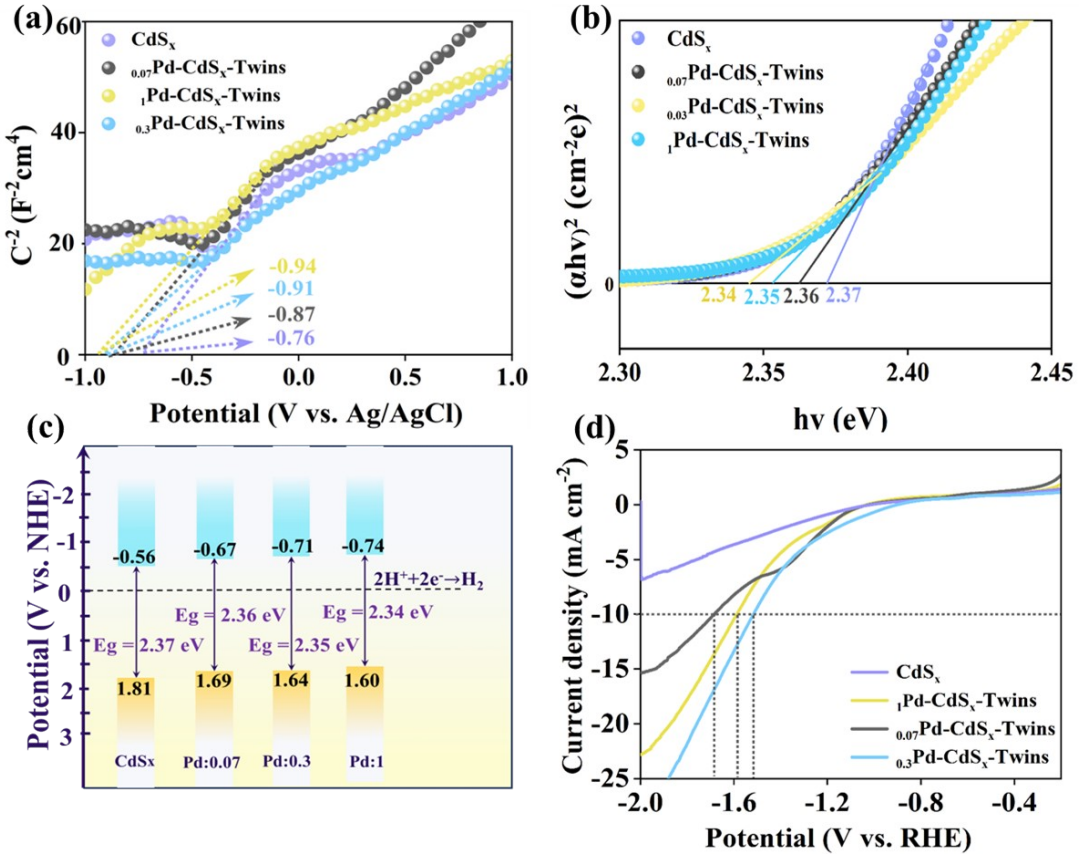

Figure S24. (a) Mott-Schottky curves and (b) linear scanning voltametric curves of Pd-CdS_x-Twins and CdS_x. (c) Energy band structure and (d) LSV curves of Pd-CdS_x-Twins and CdS_x.

Discussion: To characterize the flat band potential of the Pd-CdS_x-Twins, Mott-Schottky (MS) curves of the samples were performed through the electrochemical workstation. As shown in Supplementary Fig. S24a, the positive slope of the MS plot indicates that the prepared Pd-CdS_x-Twins are n-type semiconductors. The flat band

potential of the sample is obtained by intercepting the tangent line. Based on this, combined with the band gap values of the Pd-CdS_x-Twins (Supplementary Fig. S24b), the conduction and valence band potentials of the Pd-CdS_x-Twins are calculated (Supplementary Fig. S24c). The constant negative shift of the conduction band with increasing Pd content indicates the enhancement of the photocatalytic reduction ability.

The energy band structures of the prepared materials were calculated according to Equation S7-S8:

$$E_{NHE} = E_{Ag/AgCl} + 0.197\ V \qquad (S7)$$

$$E_{VB} = E_{CB} + E_g \qquad (S8)$$

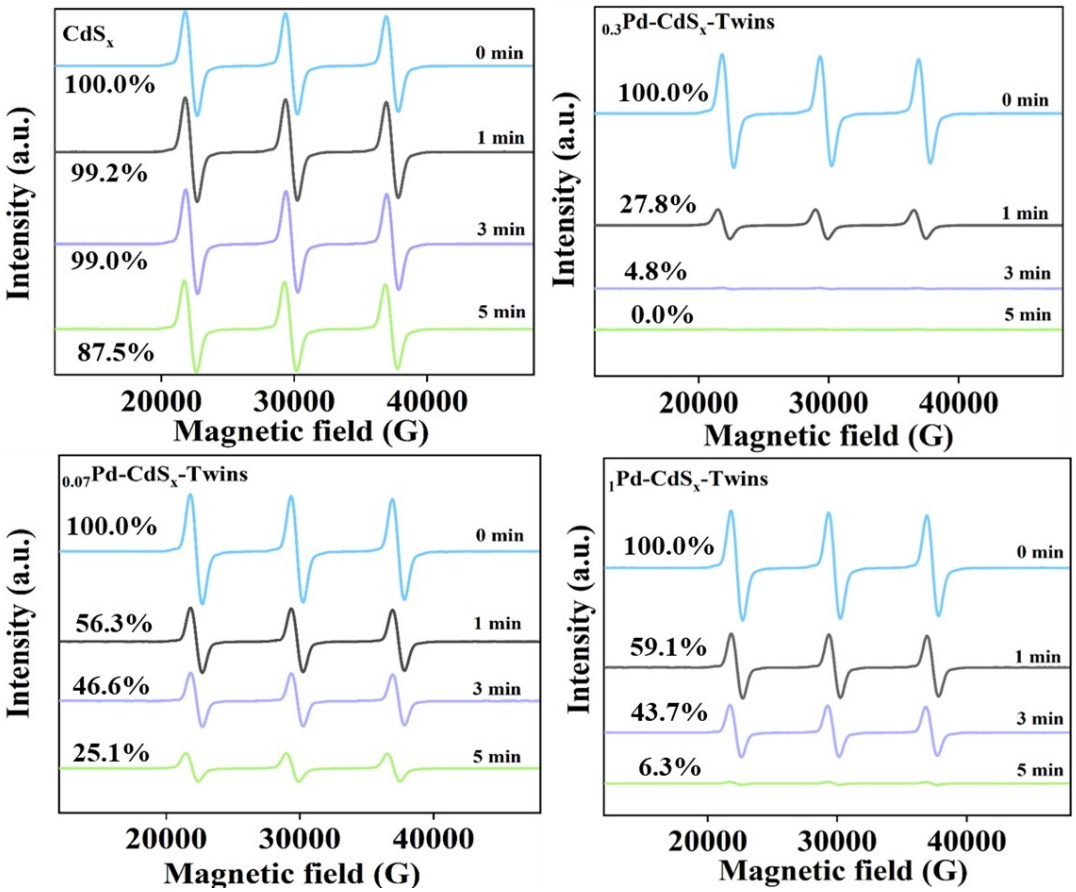

Figure S25. ESR spectra of of Pd-CdS_x-Twins and CdS_x at different time ranges (TEMPO-e-).

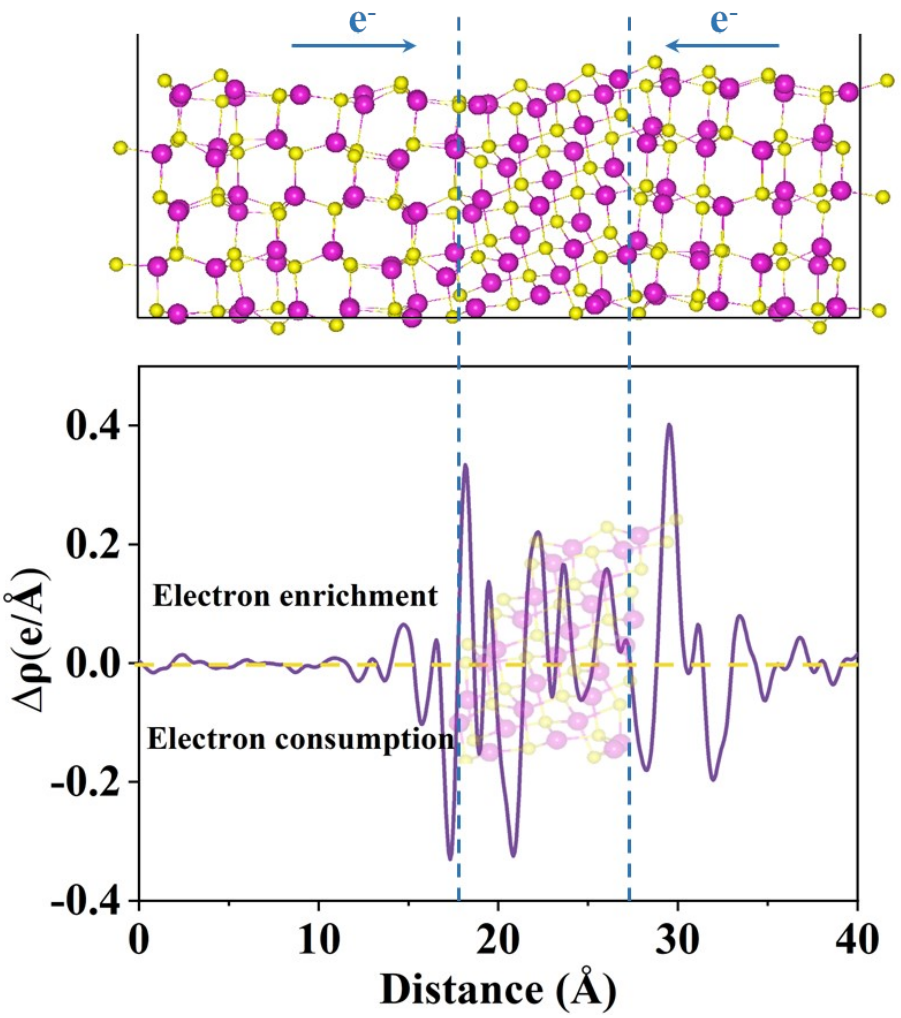

Figure S26. The plane-integrated electron density difference along the vertical direction for CdS_x-Twins (the yellow atoms are S; the pink atoms are Cd).

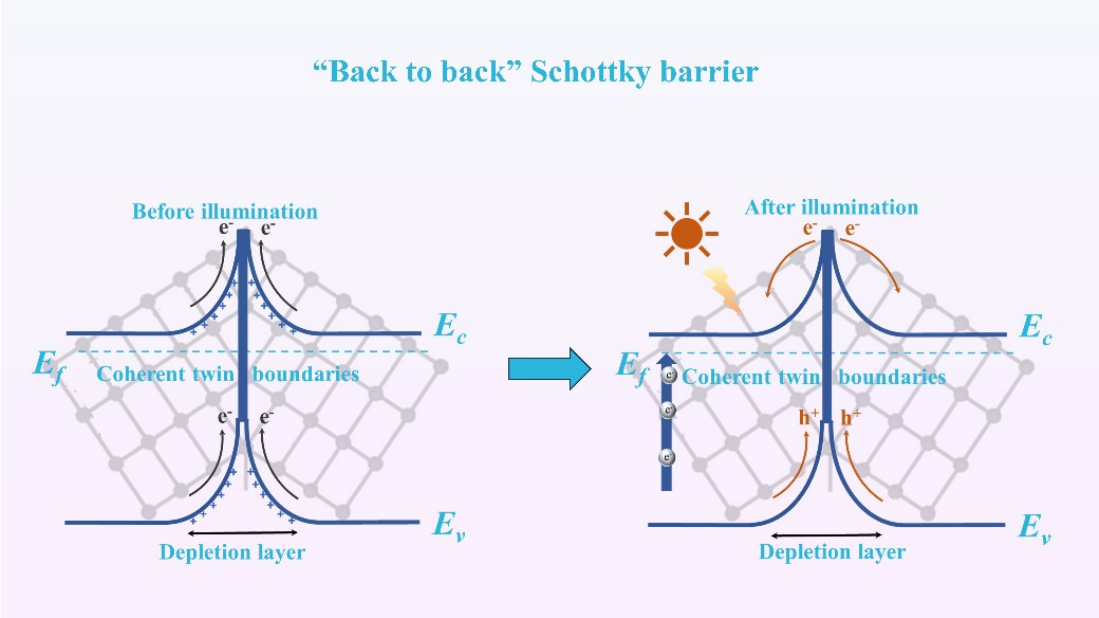

Figure S27. Back-to-back potential barrier fields of CdS_x-Twins.

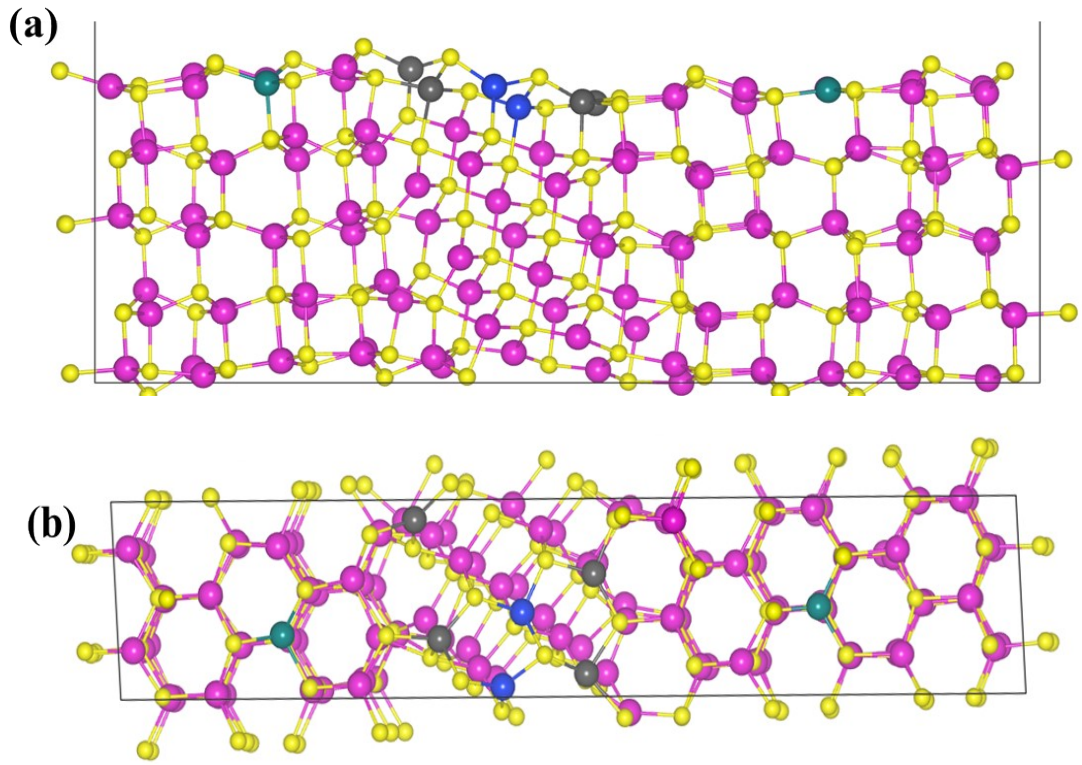

Figure S28. The calculation model of Pd-CdS_x-Twins with Pd single atoms doped at different positions of (a) cubic phase CdS and (b) hexagonal phase CdS, where yellow atoms are S atoms, pink atoms are Cd atoms, cyan, blue and gray are Pd single atoms at different positions respectively.

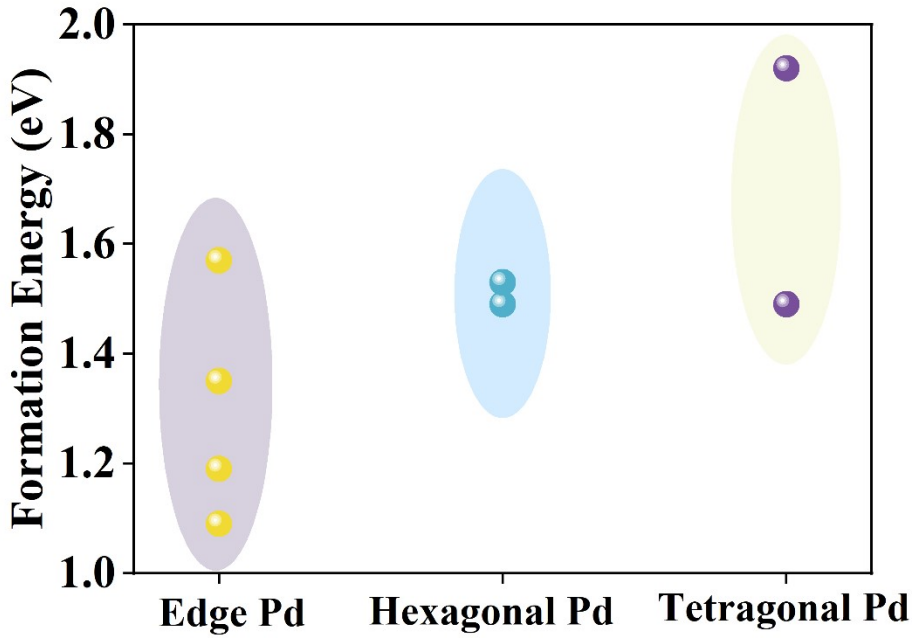

Figure S29. The formation energy profiles of Pd-CdS_x-Twins with Pd single atoms doped at different positions in the cubic and hexagonal phases of CdS.

Table S5. The table of formation energy values for Pd-CdS_x-Twins with Pd single atoms doped at different positions in cubic and hexagonal phase CdS.

edge				**hexagonal**		**cubic**	
e-1	e-2	e-3	e-4	h-1	h-2	c-1	c-2
1.09	1.35	1.57	1.19	1.49	1.53	1.49	1.92

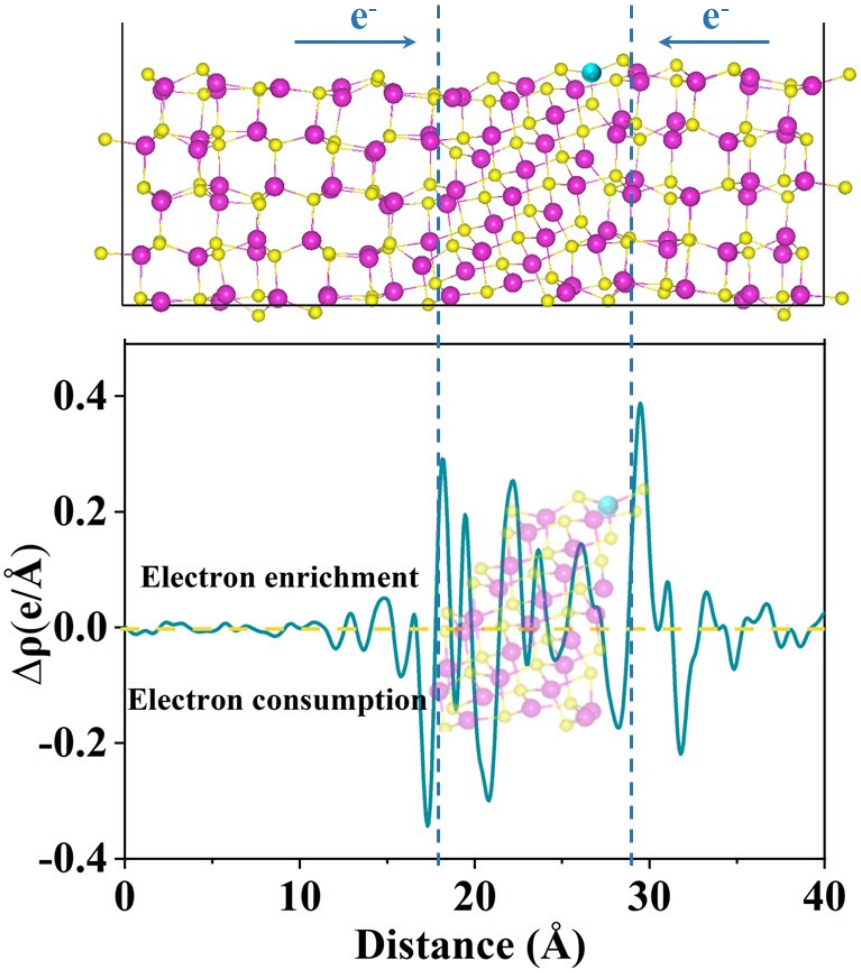

Figure S30. The plane-integrated electron density difference along the vertical direction for Pd-CdS_x-Twins (the yellow atoms are S, the pink atoms are Cd, and the cyan atoms are Pd).

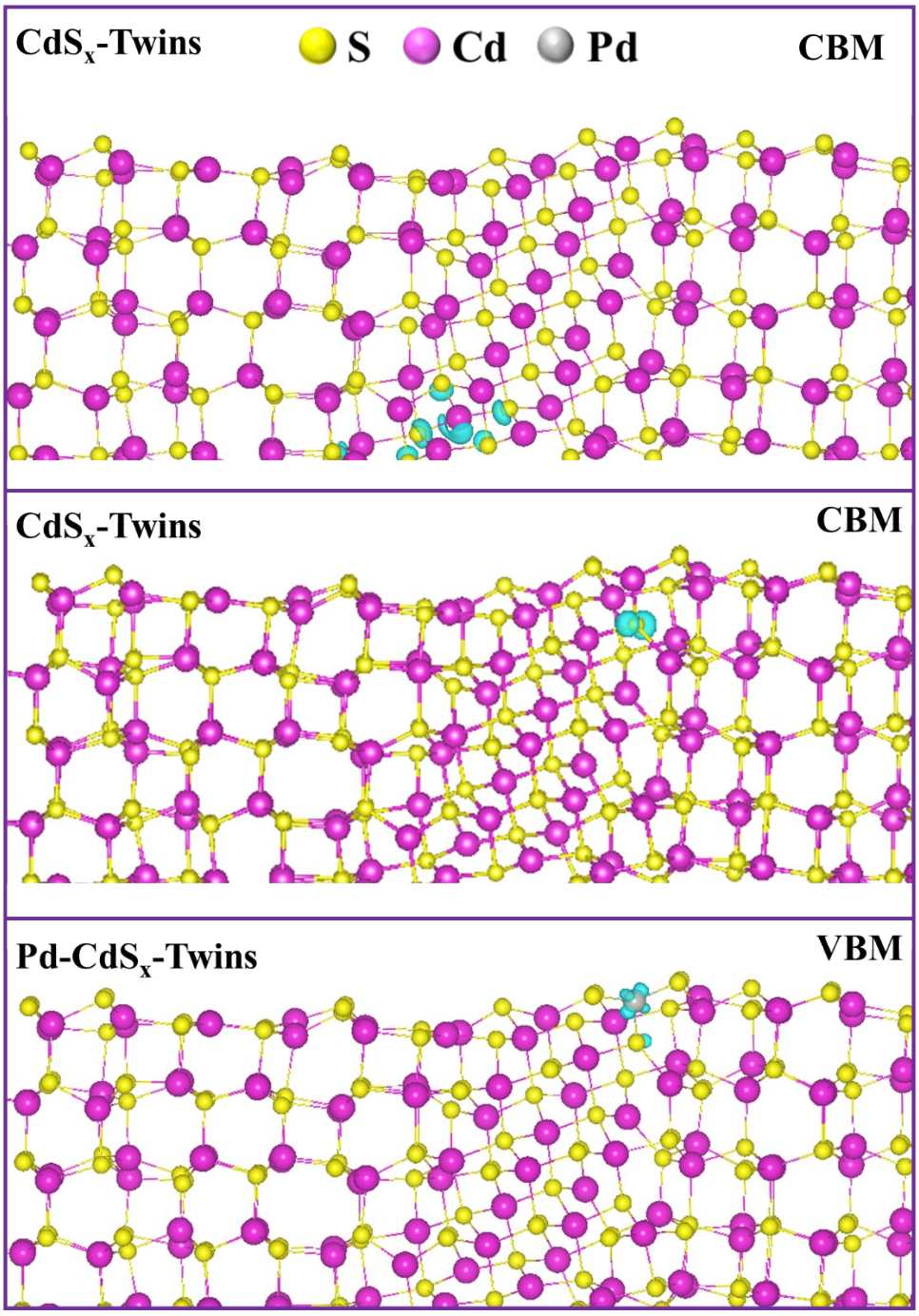

Figure S31. Calculated partial charge densities corresponding to CBM and VBM of CdS_x-Twins and VBM of Pd-CdS_x-Twins.

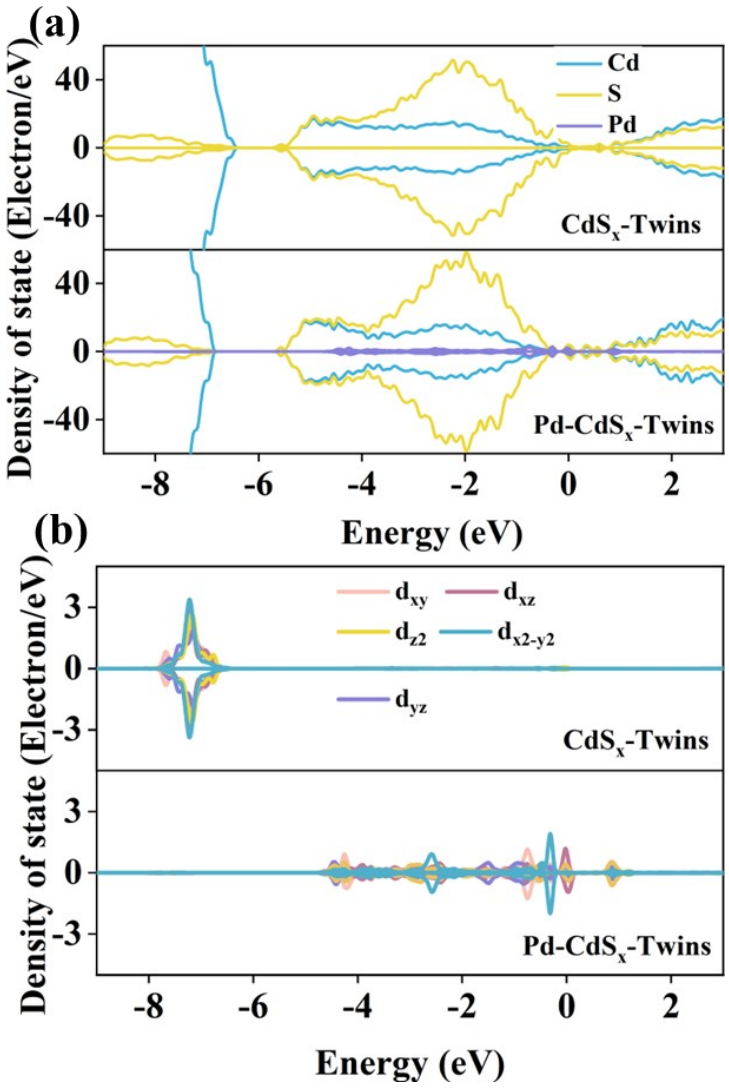

Figure S32. (a) Density of states and (b) divergent density of states for CdS_x-Twins and Pd-CdS_x-Twins.

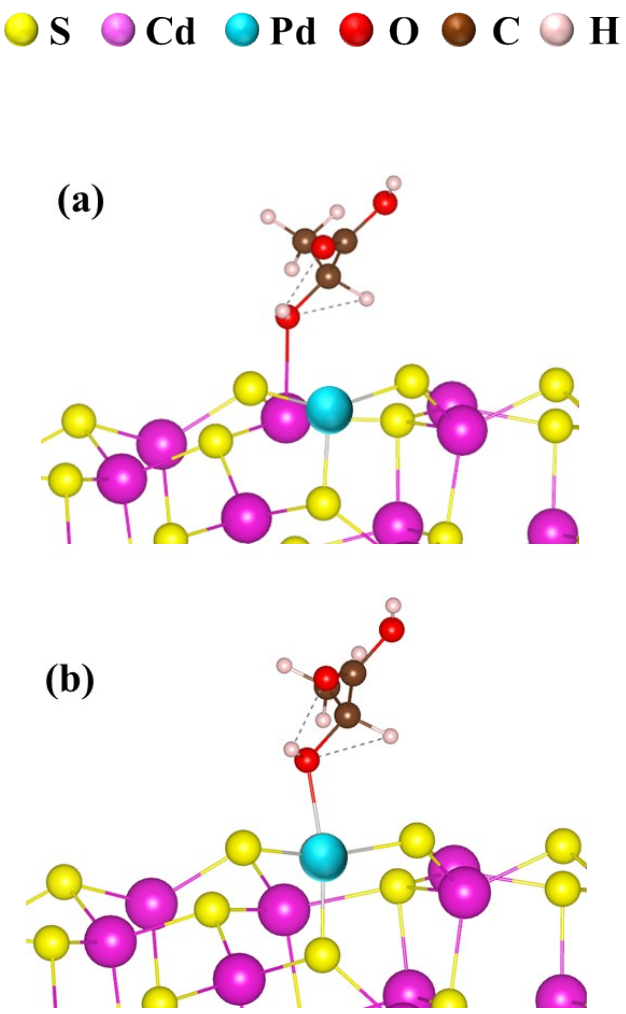

Figure S33. Lactic acid adsorption models at metal sites: (a) Cd site and (b) Pd site.

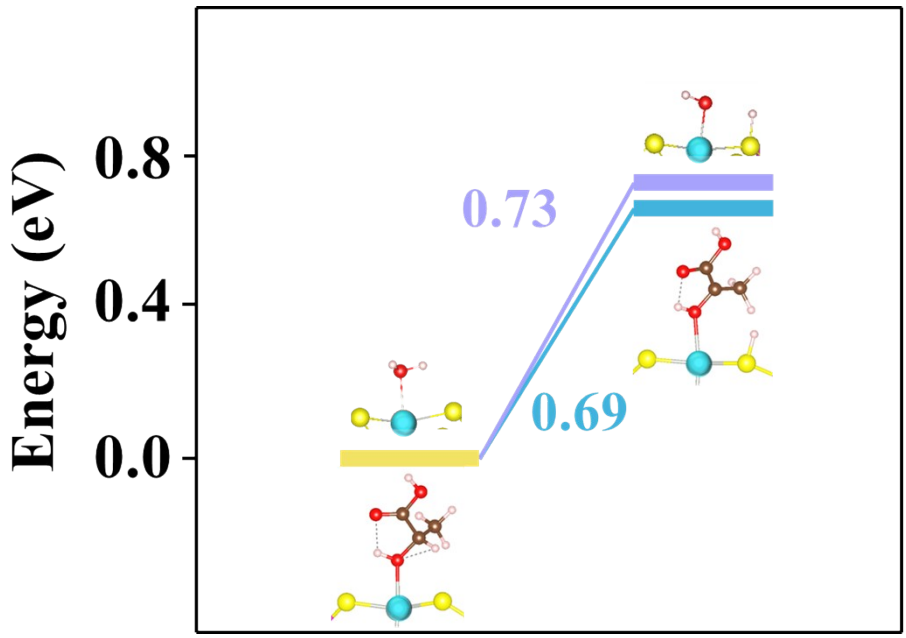

Figure S34. Energy differences in the dehydrogenation pathways of LA and water molecules on Pd-CdS_x-Twins.

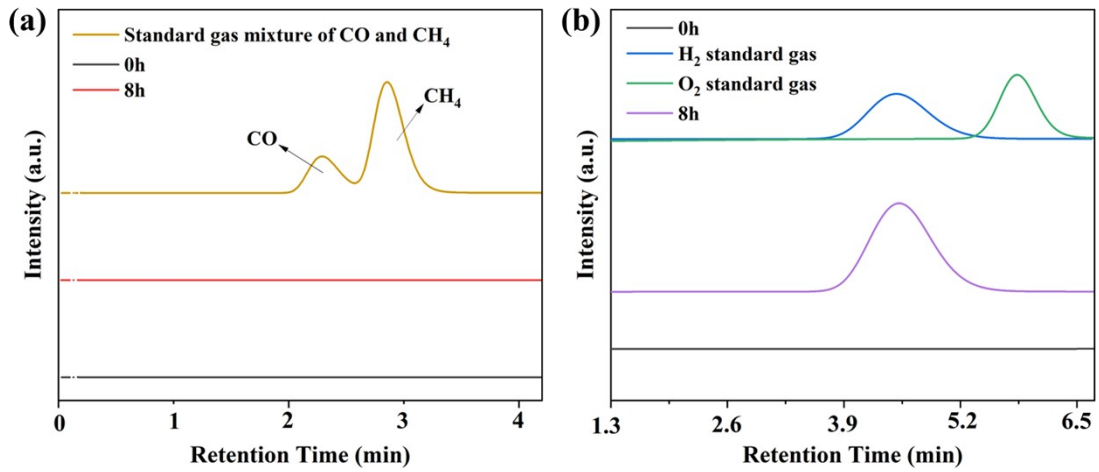

Figure S35. GC curves of gas generation of $_{0.3}$Pd-CdS$_x$-Twin and standard gas over time.

Table S6. The summary of activity reports of representative CdS-based catalysts for hydrogen production via lactic acid.

Catalyst	Lactic acid concentration	H_2 production (μmol/h)	Light source	AQE (%)	Ref.
0.2wt%MoS_2/CdS	9 vol%	540	λ > 420 nm	-	[4]
$W_{18}O_{49}$/CdS	20 vol%	1084.8	λ > 420 nm	40.06	[5]
Pt-CdS_x-T	10 vol%	854	λ > 420 nm	43.6	[6]
15%NiO/CdS@Cu_3P-X	10 vol%	156.12	5 W LED	10.4	[7]
CdS/ReS_2	10 vol%	2750	λ > 420 nm	53.6	[8]
CdS/g-C_3N_4	10 vol%	2.54	λ > 420 nm	3.41	[9]
NiCoP/CdS/NiCoPi	10 vol%	404	λ > 420 nm	3.95	[10]
(Pt/Mo_2N)/CdS	10 vol%	1.73	λ > 420 nm	-	[11]
CdS/Au-Co	10 vol%	86.46	λ > 420 nm	8.87	[12]
0.5wt%Pt/CdS	20 vol%	3.65	λ > 420 nm	46.0	[13]
CdS-cys-MoS_2	20 vol%	15.2	White light (400–720 nm)	-	[14]
0.5wt%Pt/CdS/rGO	10 vol%	4.90	λ > 420 nm	22.5	[15]
Pd-CdS_x-Twins	**10 vol% LA**	**7700.25**	**λ > 420 nm**	**90.2**	**This work**

Table S7. The summary of recent literature reports on the biomass conversion activity of lactic acid.

Catalyst	Products and properties	Light source	Selectivity (%)	Yeid of PA (%)	AQE	Ref.
$CdS/MoO_2/MoS_2$	pyruvic acid and H_2 (24 μmol/h)	λ > 420 nm	pyruvic acid (94.7)	27.1%	11.3	[16]
d-$NiPS_3$/CdS	ethylene terephthalate and H_2 (40 μmol/h)	λ > 420 nm	-		2.83	[17]
Pt/TiO_2	Acetaldehyde and H_2 (694.33 μmol/h)	500 W Hg lamp	-		-	[18]
Pd-CdS_x-Twins	**pyruvic acid and H_2 (7700.25 μmol/h)**	**λ > 420 nm**	**pyruvic acid (95.87)**	**58.5%**	**90.2**	**This work**

References

1 Tyagi, A., Matsumoto, T., Kato, T. & Yoshida, H. Direct C-H bond activation of ethers and successive C-C bond formation with benzene by a bifunctional palladium-titania photocatalyst. *Catalysis Science & Technology* **6**, 4577-4583, doi:10.1039/c5cy02290h (2016).

2 Fukui, M. *et al.* Visible light-induced diastereoselective semihydrogenation of alkynes to cis-alkenes over an organically modified titanium(IV) oxide photocatalyst having a metal co-catalyst. *Journal of Catalysis* **374**, 36-42, doi:10.1016/j.jcat.2019.04.022 (2019).

3 Tyagi, A., Yamamoto, A., Kato, T. & Yoshida, H. Bifunctional property of Pt nanoparticles deposited on TiO₂ for the photocatalytic sp³C-sp³C cross-coupling reactions between THF and alkanes. *Catalysis Science & Technology* **7**, 2616-2623, doi:10.1039/c7cy00535k (2017).

4 Zong, X. *et al.* Enhancement of photocatalytic H-2 evolution on CdS by loading MOS2 as cocatalyst under visible light irradiation. *Journal of the American Chemical Society* **130**, 7176-+, doi:10.1021/ja8007825 (2008).

5 Wang, B. *et al.* Rational designing 0D/1D Z-scheme heterojunction on CdS nanorods for efficient visible-light-driven photocatalytic H-2 evolution. *Chemical Engineering Journal* **412**, doi:10.1016/j.cej.2021.128690 (2021).

6 Tang, Y. *et al.* Surface Unsaturated Sulfur Modulates Pt Sub-Nanoparticles on Tandem Homojunction CdS for Efficient Electron Extraction. *Advanced Energy Materials* **13**, doi:10.1002/aenm.202203827 (2023).

7 Quan, Y. K., Wang, G. R., Chang, C. C. & Jin, Z. L. Co-catalyst and heterojunction dual strategies to induce photogenerated charge separation for efficient hydrogen evolution of CdS. *Nanoscale* **15**, 1186-1199, doi:10.1039/d2nr05466c (2023).

8 Ye, L. Q. *et al.* Robust and efficient photocatalytic hydrogen generation of ReS2/CdS and mechanistic study by on-line mass spectrometry and in situ infrared spectroscopy. *Applied Catalysis B-Environmental* **257**, doi:10.1016/j.apcatb.2019.117897 (2019).

9 Chen, L., Xu, Y. M. & Chen, B. In situ photochemical fabrication of CdS/g-C3N4 nanocomposites with high performance for hydrogen evolution under visible light. *Applied Catalysis B-Environmental* **256**, doi:10.1016/j.apcatb.2019.117848 (2019).

10 Zhao, Y. *et al.* Redox Dual-Cocatalyst-Modified CdS Double-Heterojunction Photocatalysts for Efficient Hydrogen Production. *Acs Applied Materials & Interfaces* **12**, 46073-46083, doi:10.1021/acsami.0c12790 (2020).

11 Ma, B., Li, X., Li, D. & Lin, K. A difunctional photocatalytic H2 evolution composite co-catalyst tailored by integration with earth-abundant material and ultralow amount of noble metal. *Applied Catalysis B: Environmental* **256**, doi:10.1016/j.apcatb.2019.117865 (2019).

12 Yi, X. Q., Li, H. T., Wang, P., Fan, J. J. & Yu, H. G. Boosting antiphotocorrosion and hydrogen-production activity of cadmium sulfide by cobalt lactate complex. *Applied Surface Science* **512**, doi:10.1016/j.apsusc.2019.144786 (2020).

13 Feng, R. *et al.* Anchoring single Pt atoms and black phosphorene dual co-catalysts on CdS nanospheres to boost visible-light photocatalytic H_2 evolution. *Nano Today* **37**, doi:10.1016/j.nantod.2021.101080 (2021).

14 Rothfuss, A. R. M. *et al.* Linker-Assisted Assembly of Ligand-Bridged CdS/MoS2 Heterostructures: Tunable Light-Harvesting Properties and Ligand-Dependent Control of

Charge-Transfer Dynamics and Photocatalytic Hydrogen Evolution. *Acs Applied Materials & Interfaces*, doi:10.1021/acsami.3c06722 (2023).

15 Li, Q. *et al.* Highly efficient visible-light-driven photocatalytic hydrogen production of CdS-cluster-decorated graphene nanosheets. *J Am Chem Soc* **133**, 10878-10884, doi:10.1021/ja2025454 (2011).

16 Bie, C. *et al.* A Bifunctional CdS/MoO2/MoS2 Catalyst Enhances Photocatalytic H2 Evolution and Pyruvic Acid Synthesis. *Angewandte Chemie International Edition* **61**, doi:10.1002/anie.202212045 (2022).

17 Zhang, S. *et al.* Boosted Photoreforming of Plastic Waste via Defect-Rich NiPS3 Nanosheets. *Journal of the American Chemical Society* **145**, 6410-6419, doi:10.1021/jacs.2c13590 (2023).

18 Liu, K. T. *et al.* Photocatalytic decarboxylation of lactic acid by Pt/TiO2. *Chemical Communications* **52**, 11634-11637, doi:10.1039/c6cc06530a (2016).